Materials Today Bio 30 (2025) 101403

Contents lists available at ScienceDirect

Materials Today Bio

journal homepage: www.journals.elsevier.com/materials-today-bio

Biomimetic ECM nerve guidance conduit with dynamic 3D interconnected porous network and sustained IGF-1 delivery for enhanced peripheral nerve regeneration and immune modulation

Teng Wan [a,b,c], Qi-Cheng Li [a,b,c], Feng-Shi Zhang [a,b,c], Xiao-Meng Zhang [a,b,c], Na Han [a,b,c,*], Pei-Xun Zhang [a,b,c,d,**]

[a] Department of Orthopedics and Trauma, Peking University People's Hospital, Beijing, 100044, China
[b] Key Laboratory of Trauma and Neural Regeneration, Peking University, Beijing, 100044, China
[c] National Centre for Trauma Medicine, Beijing, 100044, China
[d] Peking University People's Hospital Qingdao Hospital, Qingdao, 266000, China

ARTICLE INFO

Keywords:
Peripheral nerve regeneration
Interconnected porous networks
IGF-1
Macrophage polarisation
Nerve guidance conduit

ABSTRACT

Recent advancements in tissue engineering have promoted the development of nerve guidance conduits (NGCs) that significantly enhance peripheral nerve injury treatment, improving outcomes and recovery rates. However, utilising tailored biomimetic three-dimensional (3D) topological porous structures combined with multiple bioeffect neurotrophic factors to create environments similar to neural tissues, regulate local immune responses, and develop a supportive microenvironment to promote peripheral nerve regeneration and repair poses significant challenges. Herein, a biomimetic extracellular matrix (ECM) NGC featuring an interconnected 3D porous network and sustained delivery of insulin-like growth factor-1 (IGF-1) is designed using multi-functional gelatine microcapsules (GMs). Nerve conduits made by blending chitosan (CS) with GMs demonstrate suitable degradation rates, reduced swelling rates, increased suture tensile strength, improved elongation at break, and 50 % radial compression performance that meet clinical application requirements. In vitro cytological studies indicate that biomimetic ECM NGCs exhibit good biocompatibility, promote early survival, proliferation, and remyelination potential of Schwann cells (SCs), and support neurite outgrowth. The biomimetic ECM NGCs comprising a 3D interconnected porous network in a 10-mm sciatic nerve defect rat model sustain IGF-1 delivery, promoting early infiltration of macrophages and polarisation towards M2-type macrophages. Furthermore, observations at 12 weeks post-implantation revealed improvements in electrophysiological performance, alleviation of gastrocnemius muscle atrophy, increased peripheral nerve regeneration, and motor function restoration. Thus, biomimetic ECM NGCs offer a therapeutic strategy for peripheral nerve regeneration with promising clinical applications and transformation prospects to regulate immune microenvironments, promoting SC proliferation and differentiation with nerve axon growth.

Abbreviations: (NGCs), nerve guidance conduits; (3D), three-dimensional; (ECM), extracellular matrix; (IGF-1), insulin-like growth factor-1; (GMs), gelatine microcapsules; (SCs), Schwann cells; (PNI), peripheral nerve injury; (SK), shish-kebab; (CS), chitosan; (RT), room temperature; (SEM), scanning electron microscopy; (DMEM), Dulbecco's modified eagle medium; (FBS), foetal bovine serum; (HS), horse serum; (OD), optical density; (GAP), growth-associated protein; (NF), neurofilament; (PFA), paraformaldehyde; (IF), immunofluorescence; (TNF-α), tumour necrosis factor-alpha; (Arg-1), arginase-1; (CD206), cluster of differentiation 206; (iNOS), inducible nitric oxide synthase; (SD), Sprague–Dawley; (SFI), sciatic function index; (CMAP), compound muscle action potential; (NCV), nerve conduction velocity; (TEM), transmission electron microscopy; (TBS), toluidine blue staining; (SD), standard deviation; (FTIR), Fourier transform infrared spectroscopy; (NGF), nerve growth factor; (NCAM), neural cell adhesion molecule 1; (MCM), macrophage-conditioned medium; (VEGF), vascular endothelial growth factor; (NT), neurotrophin.

* Corresponding author. Department of Orthopedics and Trauma, Peking University People's Hospital, Beijing, 100044, China.
** Corresponding author. Department of Orthopedics and Trauma, Peking University People's Hospital, Beijing, 100044, China.
E-mail addresses: hannaqa@hotmail.com (N. Han), zhangpeixun@bjmu.edu.cn (P.-X. Zhang).

https://doi.org/10.1016/j.mtbio.2024.101403
Received 10 September 2024; Received in revised form 5 December 2024; Accepted 10 December 2024
Available online 12 December 2024

1. Introduction

Peripheral nerve injury (PNI) indicates damage to the structure and function of peripheral nerve fibres caused by trauma, compression, or metabolic disorders, leading to abnormal sensory, motor, and autonomic nerve functions [1]. Although partial regeneration can be achieved, repair processes have inherent limitations and are often incomplete, resulting in suboptimal functional recovery [2]. According to the clinical intervention standard of PNI, tension-free epineurium/perineurium end-to-end sutures are only suitable to bridge the gap for nerve transection injuries with defects less than 2 mm [3]. Autologous transplantation is regarded as the "gold standard" for treating peripheral nerve defects (>2 mm) due to its high compatibility and ability to support axonal regrowth. However, the method has significant disadvantages, including donor site morbidity, limited availability of donor nerves, and the potential for neuroma formation at the harvest site [4]. A promising therapeutic strategy involves the use of tissue-engineered NGCs to promote peripheral nerve regeneration. The advantages of NGCs include customisation to 3D porous structures, topological morphology, and composition to suit specific injury needs, with the potential to incorporate growth factors, cells, and ECM components for enhancing regeneration [5]. The developmental potential of NGCs lies in their capacity to integrate advanced 3D topological structures and bioactive molecules, offering a versatile and highly effective approach to PNI treatment, potentially surpassing traditional methods of functional recovery and patient outcomes [6].

The key to the successful repair of peripheral nerves by NGCs lies in their ability to provide a supportive microenvironment that facilitates SC activity, promotes axonal growth, and modulates the immune response, particularly the polarisation of macrophages towards the regenerative M2 phenotype [7,8]. Previous studies [9] have shown that SCs play a pivotal role in peripheral nerve regeneration as they clear debris, recruit macrophages, myelinate regenerated axons, deliver neurotrophic factors, and provide physical and biochemical support for axonal growth. Their activation and migration to injury sites are essential for successful nerve repair. Currently, most tissue-engineered NGCs are designed to support SC activity and enhance regenerative function [10,11]. Additionally, an immune microenvironment plays a crucial role in nerve regeneration after PNI by modulating inflammation and orchestrating cellular responses [12]. Macrophages, the primary immune-inflammatory cells that infiltrate NGCs early, are central to such an environment [13]. In response to different stimuli, macrophages exhibit either a classical activation phenotype (M1, pro-inflammatory) or an alternative activation phenotype (M2, pro-healing) [8]. Macrophages in the early stages of injury are pro-inflammatory and responsible for debris clearance and neurotrophic factor delivery [14]. As healing progresses, a phenotypic switch to M2 macrophages occurs [15]. M2 macrophages are anti-inflammatory and secrete cytokines with growth factors that promote tissue repair, SC activity, and axonal regeneration [16]. The polarisation from M1 to M2 is essential for the transition from inflammatory to regenerative phases, thereby optimising nerve repair. Currently, numerous studies [17,18] aim to promote peripheral nerve regeneration by constructing NGCs that regulate the immunophenotypic polarisation of macrophages. NGCs can be engineered with specially tailored bionic 3D topologies and bioactive molecules to promote the transition from M1 to M2 macrophages. For example, the incorporation of growth factors into NGCs can accelerate the switch to the M2 phenotype, thereby fostering a regenerative environment [19]. Additionally, NGCs can be designed to mimic the natural ECM structure and provide physical and biochemical cues to support the beneficial activities of M2 macrophages [20]. NGCs can significantly improve the efficacy of peripheral nerve repair strategies by modulating the immune microenvironment and promoting appropriate macrophage polarisation. Therefore, the primary task in designing NGC-based therapeutic strategies involves the simulation and maintenance of a dynamic supportive microenvironment conducive to peripheral nerve regeneration while effectively regulating macrophage immunophenotypes.

The biomimetic design of NGCs, particularly of those with interconnected porous networks, plays a pivotal role in peripheral nerve regeneration [21]. First, the interconnected porous network structures provide a 3D scaffold similar to the natural ECM, supporting cellular attachment, migration, and organisation [22]. Second, the interconnected porous network structure of the NGCs facilitates the diffusion of nutrients and oxygen, which are crucial for cell survival, cell function, and metabolic waste removal [23]. Additionally, by incorporating growth factors and cell adhesion molecules, the structures can replicate biochemical signals present in the ECM that guide cell behaviour and differentiation [24]. Notably, studies [25,26] have reported that the 3D topological biomimetic structure of tissue-engineered scaffolds significantly affects macrophage immunophenotypic polarisation, which is critical for creating a regenerative immune microenvironment. Dong et al. [20] used electrospun fibres to fabricate NGC with an aligned structure, which significantly promoted the transition of macrophages from pro-inflammatory M1 to anti-inflammatory M2 phenotypes. The M2 macrophages secrete anti-inflammatory cytokines and growth factors that support tissue repair and regeneration. Zhu et al. [27] used solution-induced crystallisation to form a shish-kebab (SK) structure on a material surface, creating electrospun fibre scaffolds with varying pore size and roughness. Their study demonstrated that tissue-engineered scaffolds with larger pore sizes and lower stiffness promoted macrophage polarisation towards the M2 immunophenotype. Therefore, a tailored 3D biomimetic porous structure is crucial in constructing tissue-engineered NGCs to enhance interactions between scaffolds and nerve regeneration-related cells, regulate macrophage immune phenotype polarisation, control inflammatory factor secretion, and provide a supportive microenvironment for nerve regeneration.

The application of IGF-1 in peripheral nerve regeneration and repair holds significant promise owing to its multi-faceted role in promoting neuronal health and functions [28]. Unlike other growth factors, IGF-1 offers a broad spectrum of actions that affect neurones, SCs, and other supporting cells within the nerve tissue [29]. First, IGF-1 enhances the proliferation and differentiation of SCs, which are vital for myelin sheath formation around axons [30]. Additionally, IGF-1 protects neurones from apoptosis and promotes nerve axon regeneration after injury [31]. Furthermore, the anti-inflammatory properties of IGF-1 help reduce the detrimental effects of chronic inflammation often observed after nerve injury, thereby enhancing the overall regenerative process [32]. The comprehensive approach assists in creating a more holistic, regenerative environment. One of the primary applications of IGF-1 includes the development of biomaterials and scaffolds for nerve repair [33]. Scaffolds can be embedded with IGF-1, providing localised and sustained delivery of growth factors to the injured sites [34], which helps maintain high concentrations of IGF-1 at the site to enhance its therapeutic efficacy [35].

In this study, NGCs with biomimetic ECM using CS/GMs/IGF-1 composite materials, featuring a 3D interconnected porous network and sustained delivery of IGF-1, are prepared (Schematic 1). The pore characteristics, porosity, permeability, in vitro degradation, water absorption, swelling behaviour, suture tensile properties, 50 % radial compressive performance, and IGF-1 delivery kinetics of the NGCs are systematically investigated. From in vitro cellular studies, the effects of closed non-interconnected porous structures, 3D interconnected porous networks, and 3D interconnected porous networks sustaining IGF-1 delivery NGCs on SC activation and axonal growth are examined. Subsequently, the impacts of porous connectivity and sustained IGF-1 delivery on macrophage recruitment, immune phenotype polarisation, and the effects of macrophage immune phenotype polarisation on SC migration and remyelination are systematically investigated. For in vivo studies, the biomimetic ECM NGCs are implanted into a 10 mm sciatic nerve defect rat model to explore the effects of a 3D interconnected porous network and sustained IGF-1 delivery on macrophage

recruitment, polarisation, axonal regeneration, myelination, target organ protection, and motor function recovery. This study demonstrates that ECM-mimicking NGCs with 3D interconnected porous networks and sustained IGF-1 delivery dynamically modulate macrophage immune phenotypes and provide a repair-supportive microenvironment for peripheral nerve regeneration, offering a viable nerve tissue engineering strategy for PNI repair.

2. Materials and methods

2.1. Gelatin microcapsules (GMs) synthesis and loading with IGF-1

GMs were prepared via a modified water-in-oil (w/o) emulsion method [36]. Briefly, 2 g of gelatin (Sigma-Aldrich, USA) was dissolved in 10 ml of deionized water at 55 °C for 30 min under magnetic stirring to prepare a 20 % (w/v) gelatin solution. The gelatin solution was then poured into a mixture of 200 ml soybean oil/paraffin oil (Tianjin Chemical Reagent Company, China) in a 1:4 (v/v) ratio containing 0.1 % Span 80 (Sigma-Aldrich, USA) and stirred at 55 °C, 650 rpm for 1 h to form a homogeneous emulsion. The emulsion was rapidly submerged into liquid nitrogen, causing rapid fixation and formation of GMs. Finally, the GMs were collected via centrifugation and washed three times alternately with acetone and PBS.

For cross-linking, GMs were suspended in a 50 % aqueous ethanol solution containing 0.5 wt% genipin (Sigma-Aldrich, USA) at 4 °C for varying durations (4, 8, 12, and 24 h), yielding CL-4h, CL-8h, CL-12h, and CL-24h, respectively. After centrifugation and washing, GMs were freeze-dried and sieved to sizes of 20–80 μm. IGF-1 (Aladdin, USA) was loaded into GMs by soaking them in PBS (pH 7.4) for 6 h at 4 °C, followed by washing with a 10 mg/ml albumin solution. The loading efficiency was quantified using an ELISA kit (Abcam, USA).

2.2. Fabrication of CS/GMs biomimetic ECM NGCs

The process for preparing the NGCs is shown in Schematic 1. The 4 h and 24 h cross-linked GMs (both loaded and unloaded with IGF-1) were mixed in a 1:1 mass ratio to create multifunctional GMs. Chitosan (CS) was dissolved in a 0.08 M acetic acid solution to prepare a 5 % (w/v) CS solution. To fabricate 3D interconnected porous NGCs, 0.5, 0.75, and 1 g of multifunctional GMs were blended into 20 ml of 5 % CS solution at 4 °C under ultrasonic conditions. For non-interconnected structures, 0.75 g of pure gelatin was added to 20 ml of 5 % CS solution, dissolved at 40 °C, and mixed thoroughly. The solution was ultrasonically treated to remove bubbles, injected into molds, and pre-cooled at −20 °C and −40 °C for 6 h before freezing at −80 °C for an additional 6 h. The NGCs were neutralized in a 4 % (w/v) NaOH solution for 1 h, rinsed with

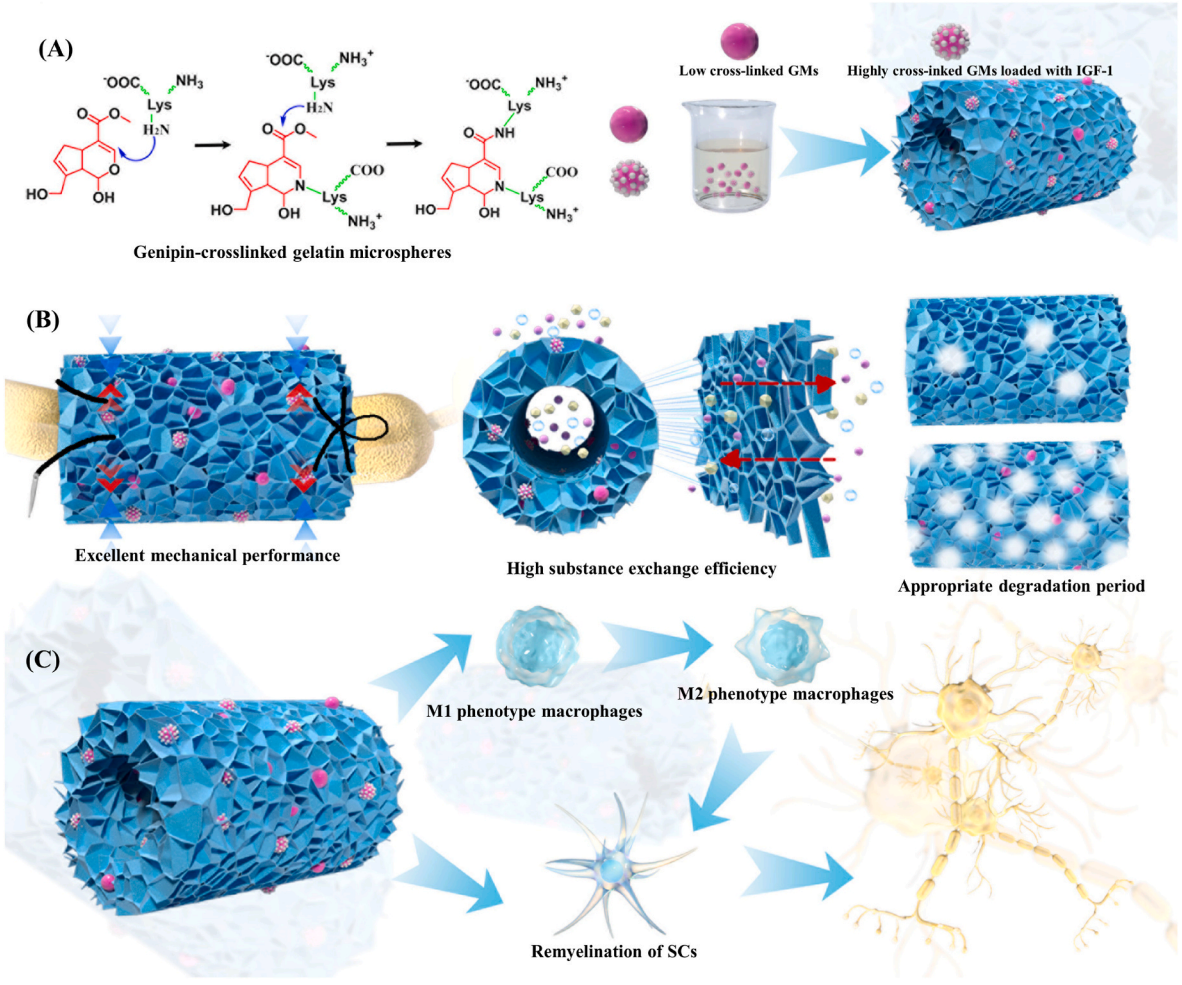

Schematic 1. illustrates the preparation, properties, and promotion of peripheral nerve regeneration by the biomimetic ECM NGC. (A) Multifunctional GMs with varying degrees of crosslinking facilitate the sustained delivery of IGF-1 and the formation of an interconnected porous network structure. (B) Compared to gelatin/chitosan conduits, the multifunctional GMs/chitosan NGCs demonstrates superior suture tensile strength, elongation at break, radial compression strength, and material exchange efficiency, with a degradation rate that aligns with the peripheral nerve regeneration process. (C) The biomimetic ECM NGC promotes SC remyelination and nerve axon regrowth, modulates macrophage immune phenotypes, and provides a favorable immunological microenvironment for peripheral nerve regeneration, facilitating repair.

deionized water, freeze-dried, and stored in glycerol.

2.3. Characterisation of NGC

2.3.1. Porous structure and porosity characteristics

Scanning electron microscopy (SEM, JEOL Ltd., Japan) was used to examine the morphologies and pore structures of the NGCs. Image J software quantified the number of pores and their cross-sectional area ratios across five cross-sections, and the size distribution of pores was analysed. Dynamic variations in the porosity of the NGCs over different time intervals (6, 12, 24, 48, 72 and 96 h) in the phosphate buffer solution (PBS) solution were investigated using the ethanol displacement method. Initially, the NGC was immersed in a pre-determined volume (V_1) of anhydrous ethanol, followed by infiltration of the liquid into the conduit pores through a series of vacuum delivery cycles, resulting in a total solution volume of V_2. Subsequently, the NGC was removed, and the volume of the ethanol solution (V_3) was measured. Finally, the porosity of the NGCs was calculated as:

$$\text{Porosity rate} = \frac{V_1\text{-}V_3}{V_2\text{-}V_3} \times 100\%$$

2.3.2. Permeability kinetics studies

To evaluate permeability, a membrane (1.2 mm thick) was affixed to a 2 mL ampoule containing iodine solution (0.1 mol/mL). The ampoule was immersed in 5 mL of starch solution (1 mg/mL) at 37 °C. At intervals (6, 12, 24, 36, 48, and 72 h), absorbance was measured at 610 nm using a spectrophotometer (Tecan Infinite M200, Switzerland).

2.3.3. In vitro degradation

The in vitro degradation rate of the NGCs with different GM doping ratios was investigated using a weighing method. First, NGC of known mass (M_0) was placed in 5 mL of 0.5 U/mL type II collagenase solution in a shaker at 37 °C. The NGC was removed after the predetermined time (1, 2, 3, 5, 7, 14, 28, 42, 56, 70, and 84 d), rinsed repeatedly with deionized water, weighed (M_1) after freeze-drying, and replaced with the original PBS solution. The NGC degradation rate was calculated as:

$$\text{Degradation rate} = \frac{M_0 - M_1}{M_0} \times 100\%$$

2.3.4. Suture tensile and 50 % radial compressive mechanical properties

To investigate the effect of different GM doping ratios on the mechanical performance of the NGCs, the suture tensile and 50 % radial compressive strengths of the NGCs were studied after their complete immersion in PBS solution for 30 min at RT. An 8-0 surgical suture, consistent with clinical use, was passed 2 mm below the edge of one end of the sample and sutured in a half-loop. The other end of the sample was fixed to the sensor clamp, and the sutures were stretched at a steady speed (10 mm/min). The tensile force that pulled the suture out of the sample or caused damage to the sample and suture size were recorded.

The inner diameter (1.5 mm) of the sample was recorded. The sample was placed in the middle of a universal testing machine press, which was in contact with the sample, and pressed down at a stable speed (1 mm/s). The radial displacement of the NGC body was half the inner diameter of the NGC. The maximum pressure that the tube could withstand was recorded.

The bending strength of the nerve conduit was assessed using a three-point bending apparatus. The conduits were positioned horizontally on two supports, ensuring equal spacing. A loading rod was placed at the midpoint of the conduit. A controlled force was applied vertically at the midpoint using a mechanical testing machine, with the load gradually increased until failure.

2.3.5. Swelling measurements

The swelling ratio of the prepared NGCs (outer diameter: 2.7 mm, inner diameter: 1.5 × 14 mm) was investigated according to ASTM D570-98. Initially, the prepared NGC was thoroughly freeze-dried and weighed to determine the mass, which was recorded as M_0. Then, the NGC was immersed in a PBS solution at 37 °C. At predetermined time intervals (1, 3, 6, 12, 24, 48, and 72 h), the NGC was removed, wiped to remove residual surface water using dust-free absorbent paper, weighed, and recorded as M_1. The swelling ratio was calculated as:

$$\text{Swelling rate} = \frac{M_1\text{-}M_0}{M_0} \times 100\%$$

2.3.6. IGF-1 releasing kinetics

An enzyme-linked immunosorbent assay (ELISA; Solarbio, China) was used to investigate the kinetics of the sustained delivery of IGF-1 in vitro. Initially, NGCs (2.7 × 1.5 × 14 mm) loaded with IGF-1 were placed in a 5 mL PBS solution at 37 °C in a shaker. Subsequently, IGF-1 concentrations were measured at predetermined time intervals (1, 2, 4, 6, 10, 16, 24, 32, and 36 d) following the manufacturer's protocol.

2.4. In vitro grouping scheme and cell culture

Rat SCs (RSC96), undifferentiated murine pheochromocytoma neuronal (PC12) cells, and murine macrophage (RAW 264.7) cells were purchased from the Cell Resource Centre in Beijing, China. RSC96 and RAW264.7 cells were cultured in Dulbecco's modified eagle medium (DMEM, Invitrogen Gibco, USA), supplemented with 10 % foetal bovine serum (FBS, Invitrogen Gibco, USA), and 1 % penicillin/streptomycin (50 U/mL, Invitrogen Gibco, USA) in a 5 % CO_2 incubator at 37 °C. PC12 cells were cultured in RPMI-1640 medium (PM150110, Invitrogen Gibco, USA), supplemented with 15 % horse serum (HS, Invitrogen Gibco, USA), 5 % foetal bovine serum (FBS, Invitrogen, Gibco, USA), and 1 % penicillin/streptomycin in a 5 % CO_2 incubator at 37 °C.

The biocompatibility of different samples was evaluated through an extraction experiment using the CCK-8 assay and a live/dead cell staining kit (Calcein-AM/PI, Aigma-Aldrich, USA). NGCs were immersed in a sterile complete medium at a ratio of 6 cm^2/mL and incubated at 37 °C for extraction periods of 24 and 72 h. RSC96 cells were seeded in 96-well plates at a density of 8 × 10^3 cells/well. After 24 h of incubation, the medium was replaced with 200 μL/well of the extraction solution. Following an additional 24 h of incubation, 10 μL of CCK-8 solution (Aigma-Aldrich, USA) was added, and the plates were incubated for another 2 h. The optical density (OD) was measured at 450 nm, with complete cell culture medium serving as a control. Additionally, RSC96 cells were seeded on the membrane samples at 2 × 10^4 cells/well, cultured for 24 and 72 h according to the manufacturer's protocol, and observed under a confocal microscope (CLSM, Leica TCS SP5, Germany).

2.4.1. Proliferation and differentiation of RSC96 cells

The proliferation of RSC96 cells (2 × 10^4/well) in various samples was assessed on 1, 3, and 7 d using the CCK-8 assay. At each observation time interval, 10 μL of CCK-8 solution was added to each well that contained 90 μL of serum-free medium, followed by incubation at 37 °C for 2 h. The ODs of the samples were measured at 450 nm using a microplate reader (Tecan Infinite M200, Switzerland) to obtain absorbance readings.

The transcriptional levels of myelination-related genes, including peripheral myelin protein 22 (PMP22), nerve growth factor (NGF), and neural cell adhesion molecule 1 (NCAM), in RSC96 cells following different treatments, were examined using qRT-PCR. Cells were harvested at designated time intervals, and total RNA was extracted using AG RNAex pro reagent (Accurate Biology, China). Subsequently, cDNA synthesis was performed using PrimeScript real time master mix (Aigma-Aldrich, USA) with 1 μg of RNA in a 20 μL reaction volume. Gene expression levels were quantified by qRT-PCR using SYBR green real-time PCR master mix (Thermofisher, USA) with cycling conditions: initial denaturation at 95 °C for 60 s, followed by 40 cycles of denaturation at 95 °C for 15 s, annealing at 60 °C for 15 s, and extension at

72 °C for 45 s. The primer sequences are presented in Table S1 (Supplementary, Table 1). The relative gene expression levels were determined using the $2^{-\Delta\Delta Ct}$ method, with GAPDH gene expression serving as an endogenous control for normalisation.

2.4.2. Differentiation of PC12 cells

PC12 cells were used to evaluate the ability of various samples to promote neurite outgrowth. PC12 cells were seeded at a density of 2×10^4 cells/well in polylysine-coated samples (Sigma-Aldrich, USA). After 1, 3, 5, and 9 d of culture, the cells were stained with FITC-phalloidin and 4',6-diamidino-2-phenylindole (DAPI, Sigma-Aldrich, USA) and then imaged using a confocal laser scanning microscope (Leica TCS SP5, Germany). The levels of neuronal differentiation-related genes, growth-associated protein 43 (GAP-43) and neurofilament 200 (NF-200), relative to the control gene GAPDH in individual groups of PC12 cells were quantified by qRT-PCR, as discussed in Section 2.3.1.

2.4.3. Recruitment and polarisation of macrophages

The recruitment of macrophages (RAW 264.7 cells) was verified using a transwell co-culture system (24-well plate and 8 μm porous filter, Corning, USA). First, RSC96 cells were seeded onto the membrane of the lower chamber at a density of 2×10^4 cells/well in 700 μL of complete medium. After incubating for 12 h until the cells were fully adherent, the medium in the lower chamber was replaced with a serum-free medium. The upper chamber was seeded with 1×10^5 RAW 264.7 cells in 200 μL serum-free medium per well. After 24 h of culture, the cells were fixed with 4 % paraformaldehyde (PFA, Solarbio, China) and stained with crystal violet. Cells that did not migrate to the lower membrane were removed using a cotton swab, and the macrophages that migrated to the lower membrane were observed and recorded under a light microscope (Leica DM3000, Germany).

Immunofluorescence (IF) staining was used to examine the morphology of macrophage polarisation following culture with different samples. RAW 264.7 cells were initially seeded onto the samples at a density of 2×10^4 cells/well in 24-well plates. The RAW 264.7 cells in the control group were cultured in DMEM, while cells in the experimental groups were cultured in DMEM supplemented with 1 μg/mL of LPS. After 3 d of culture, the samples were fixed with 4 % PFA for 30 min, permeabilised with permeabilisation buffer (Beyotime, China) for 10 min, and then blocked with blocking buffer (Beyotime, China) for 1 h at RT. Subsequently, the cells were incubated for 12 h with primary antibodies, including rabbit anti-iNOS (1:2000, Abcam, USA) and rabbit anti-Arg-1 (1:2000, Abcam, USA). Thereafter, secondary antibodies of 488-conjugated goat anti-rabbit IgG (1:400, Abcam, USA) and 594-conjugated goat anti-rabbit IgG (1:400, Abcam, USA) were applied for 1 h at RT. Finally, the nuclei were counterstained with DAPI (Sigma-Aldrich), and the samples were visualised using CLSM (Leica TCS SP5, Germany).

Flow cytometry was employed to investigate the impact of the 3D interconnected porous network and sustained IGF-1 delivery on the immunophenotype of the macrophages. The cells were treated following the same protocol as described for IF. After 24 h of incubation, the RAW 264.7 cells were harvested and stained with anti-CD86 antibody (1:500, Abcam, USA) and anti-CD206 antibody (4 μL/ml, Abcam, USA) at RT for 30 min. Macrophage clusters were examined by flow cytometry (Beckman Coulter, USA) and analysed using FlowJo software (TreeStar, USA).

The relative expression levels of anti-inflammatory and pro-inflammatory genes during macrophage polarisation towards M1 or M2 phenotypes were determined using qRT-PCR. The RAW264.7 cells were processed as aforementioned. After 3 d of incubation, the relative mRNA transcript levels of tumour necrosis factor-alpha (TNF-α), arginase-1 (Arg-1), cluster of differentiation 206 (CD206), and inducible nitric oxide synthase (iNOS) genes in different groups of RAW264.7 cells were quantified relative to the control GAPDH.

The cytokine secretions of RAW 264.7 cells during polarisation towards M1 or M2 phenotypes were evaluated using mouse IL-10, IL-6, IL-13 and TNF-α ELISA kits (ThermoFisher, USA). After 3 d of culture, the culture supernatant was collected and centrifuged for detection according to the manufacturer's protocol.

2.4.4. Influence of polarised macrophages on the migration and myelination of RSC96 cells

To characterise the effect of macrophage polarisation on the longitudinal migration of SCs, a transwell co-culture system (24-well plate and 8 μm porous filter; Corning, USA) was used, as depicted in Fig. 4A. Different groups of sample membranes were placed in the lower chamber and seeded with RAW264.7 cells at a density of 2×10^4 cells/well with 700 μL of complete culture medium. The cells were incubated for 12 h to allow complete cell attachment. After 3 d of LPS stimulation, the medium was replaced with a fresh serum-free medium. The upper compartment was seeded with RSC96 cells (1×10^5 cells in 200 μL of serum-free medium/well) and allowed to migrate for an additional 24 h.

The effect of macrophage polarisation on the horizontal migration of SCs was evaluated using a wound-healing assay. RAW264.7 cells were initially seeded in six-well plates at a density of 2×10^5 cells/well on different membrane samples. After incubating for 6 h until they were fully adherent, the cells were incubated in the serum-free medium (with or without 1 μg/mL LPS) for an additional 3 d. Meanwhile, RSC96 cells were plated in six well plates at a density of 4×10^5 cells/well and incubated for 12 h until they reached 90–100 % confluency. For each experiment, the same 200 μL sterile pipette tip (Axygen, USA) was used to scratch the cell layer, creating a standardized 'wound' in the center of each well with the help of a ruler, ensuring relative consistency between groups in each experiment. The medium of the RSC96 cells was replaced with the medium from RAW264.7 cells in intervals of 12, 24, and 48 h. Cell migration was observed and recorded at the designated time intervals using an optical microscope (Leica DM3000, Germany). The wound closure areas in at least five wells/group were calculated using ImageJ J 8.0.

The effects of macrophage polarisation on the elongation of cytoskeletal actin filament and myelination-related mRNA expression in SCs were investigated using phalloidin IF staining and qRT-PCR, respectively. RAW264.7 cells were seeded onto sample membranes at a density of 2×10^5 cells/well in a complete medium. After 12 h of incubation, when the cells were fully adherent, the medium was replaced with the serum-free medium, and the cells were incubated for an additional 3 d. The medium from the RAW264.7 cells was transferred to the RSC96 cell culture system. After 24 h, the cells were fixed with 4 % PFA and stained for intracellular actin microfilaments and nuclei using FITC-labeled phalloidin and DAPI.

2.5. Animal surgery and grouping scheme

A 10 mm sciatic nerve defect rat model was established to evaluate peripheral nerve regeneration following the implantation of the biomimetic ECM NGC. Animal experimental protocols were approved by the Animal Experiment Ethics Committee of Peking University People's Hospital, China, and designed in accordance with the Animal Research: Reporting of In Vivo Experiments (ARRIVE) guidelines. A total of 110 female Sprague–Dawley (SD) rats (weighing 280–320 g) were obtained from the Experimental Animal Centre of Peking University People's Hospital (Table 1). The rats were housed in a specific pathogen-free facility under controlled conditions: temperature 22 ± 2 °C, humidity

Table 1
Experimental animal groups.

Group	Time		
	1 weeks	2 weeks	12 weeks
Autograft			11
CS/G	11	11	11
CS/GMs	11	11	11
CS/GMs @IGF-1	11	11	11

55 ± 5 %, 12 h light/dark cycle, and free access to water and food. Anaesthesia was induced and maintained using 5 % isoflurane and 1.5–2% isoflurane, respectively. Rats were placed in the prone position on the operating table, and the right thigh area was prepared and sterilised. The skin of the right leg was incised, and the subcutaneous and muscular tissues were bluntly dissected to expose the right sciatic nerve. A 10 mm sciatic nerve defect was created by transecting the sciatic nerve from the inferior border of the piriformis. Then, the NGC (length, inner diameter, and external diameter of 14, 1.5, and 2.7 mm, respectively) was sutured to the proximal and distal nerve stumps using a 10-0 suture. In the nerve autograft group, a 10 mm segment of the sciatic nerve was harvested, reversed by 180°, and sutured to the epineurium at both nerve stumps. The muscles and skin were closed with 6-0 and 4-0 sutures to complete the surgical incision, respectively. All rats were housed, fed under standard conditions, and euthanised at designated time intervals.

2.5.1. Walking track assessment

Postoperatively at 12 w, appropriate gait parameters were selected according to the experimental requirements. The SD rats were placed on the CatWalk XT runway, and data were recorded. As shown in Fig. 7J, the recorded parameters included: print length (PL; distance from the heel to the third toe), toe spread (TS; distance from the first to fifth toes), and intermediate toe spread IT (distance between the middle of the second and fourth toes). Data were collected for both experimental (E) and normal (N) hind legs. The sciatic function index (SFI) values were calculated as

$$SFI = -38.3 \times \frac{EPL-NPL}{NPL} + 109.5 \times \frac{ETS-NTS}{NTS} + 13.3 \times \frac{EIT-NIT}{NIT} - 8.8$$

The SFI values ranged from −100 to 0, where −100 indicates total impairment and 0 indicates normal function.

2.5.2. Electrophysiology assessment

Electrophysiology was used to observe the functional recovery of the regenerated nerve at 12 w post-surgery. Briefly, the sciatic nerve on the experimental side was re-exposed and dissected under anaesthesia. Rectangular pulses (parameters: duration 0.1 ms, amplitude 0.12 mA, frequency 1 Hz) were applied to the proximal and distal ends of the tibialis anterior muscle, with the ground electrode placed at the ipsilateral gluteus maximus muscle. Stimulation was repeated twice for each animal, and records were saved once the graphics on the display stabilised. The peak values of the compound muscle action potential (CMAP) and time to deflection (latency) were measured. The motor nerve conduction velocity (NCV) was calculated based on the distance between the latency period and the stimulating electrodes on both sides.

2.5.3. Evaluation of gastrocnemius muscle

Gastrocnemius muscles from both the experimental (M_1) and control sides (M_0) were dissected from individual rats and weighed. The muscle wet weight ratio (%) was calculated: (M_1/M_0) × 100 %. The middle segment of the gastrocnemius muscle was fixed in 4 % PFA for 48 h, dehydrated in an ethanol gradient (95, 80, 75 %) for 60 s, cleared in xylene, embedded in paraffin (Leica, Germany), and cut into 7 μm-thick sections. Masson's trichrome and H&E staining was performed to examine the pathological changes in the muscles. Images were obtained using an optical microscope (Leica DM3000, Germany) under bright-field conditions.

2.5.4. Histologic, morphologic, immunohistochemical, and immunofluorescent evaluation of regenerated nerves

Postoperatively at 1 and 2 w, IF was used to investigate the relationship between macrophage immune phenotypes and SCs in vivo. NGC sections were selected from 2 mm distal to the proximal suture site for staining and analysis. Frozen sections were removed from the −20 °C refrigerator, allowed to thaw at RT for 1 h, fixed with 4 % PFA for 20 min and washed repeatedly with PBS solution. The tissues were permeabilised with 0.2 % Triton X-100 for 20 min, and washed three times with PBS solution. Then, they were blocked with 10 % goat serum for 40 min at RT. Primary antibodies, including rabbit anti-S100β (1:200, Abcam), mouse anti-CD68 (1:200, Abcam, USA), rabbit anti-iNOS (1:200, Proteintech, USA) and rabbit anti-CD206 antibody (1:200, Abcam, USA), were added and incubated overnight at 4 °C. Secondary antibodies, including 488-conjugated goat anti-mouse IgG (1:400, Proteintech, USA), and 594-conjugated goat anti-rabbit IgG (1:500, Proteintech), were added. Images were visualised and captured using LSCM.

Transmission electron microscopy (TEM), toluidine blue staining (TBS), and IF were used to analyse the regeneration of peripheral nerves collected 2 mm from the distal suture site, 12 w postoperatively. For TEM and TBS, the regenerated nerves were fixed in 4 % PFA for 6 h, followed by post-fixation in 1 % osmium tetroxide for 3 h and dehydration in a series of graded ethanol solutions (30, 50, 70, 90, and 100 %). After embedding in epoxy resin and freezing in liquid nitrogen, the samples were cut into 700- or 70-nm-thick sections using an ultramicrotome (Leica, Germany). The 700 nm semi-thin sections were stained with a 1 % toluidine blue/1 % borax solution to observe the amount of regenerated myelin. Ultra-thin sections were stained with lead citrate and uranyl acetate for TEM. For IF, regenerated nerves were fixed in 4 % PFA, embedded in OCT, and sectioned into 10 μm-thick slices. Sections were blocked with 10 % goat serum for 40 min at RT and incubated overnight at 4 °C with primary antibodies against NF200 (1:400, Abcam, USA) and S100β (1:500, Abcam, USA).

2.6. Statistical analysis

Each experiment was conducted three times or more, and the data were expressed as mean ± standard deviation (SD). All statistical analyses were performed using SPSS (version 23.0; IBM Corp., USA). Comparisons between and among groups were performed using the unpaired Student's t-test, one-way ANOVA, and Tukey's method. Statistical significance was set to p-value<0.05.

3. Results

3.1. Characterisation of 3D interconnected porous network for sustained IGF-1 delivery CS-GMs conduit

3.1.1. Porous structure, porosity, and permeability

To construct the 3D interconnected porous network structure, we combined freeze-drying and template leaching to prepare a biomimetic ECM NGC using CS and multi-functional GMs, as shown in Fig. 1A. SEM observations (Fig. 1A and B) indicated that the freeze-drying method allowed the construction of a honeycomb-like porous structure in the CS/GM composite nerve conduit. The porous structure featured isolated pores with non-interconnectivity (Fig. 1C) because the procedure of freeze-drying involved freezing a crystalline polymer solution and then sublimating the crystalline ice directly from solid to gas under vacuum and low temperatures, leaving behind voids that formed a honeycomb-like porous structure [37]. Although the method produced highly porous scaffolds, the honeycomb-like porous structure obtained through the direct sublimation of solid ice crystals lacked openness and interconnectedness between the pores [38]. Additionally, doping CS with GMs at mass ratios of 1:0.50, 1:0.75, and 1:1.00 did not significantly affect the formation of honeycomb-like, non-interconnected porous structures. As shown in Fig. 1C, the GMs were embedded in the walls of the porous structure, making the smooth pore walls rough after doping. The number of pores per coronal plane, pore size distribution, and ratio of pore structures in the coronal plane were analysed using ImageJ. The number of pores per coronal plane remained consistent at 417 ± 11, 417 ± 20, 418 ± 16, and 417 ± 19 (Fig. 1D), while the distribution of pore sizes was 10.6–71.5, 10.4–72.4, 10.1–70.9, and 11.2–71.2 μm (Fig. 1E), respectively. The ratio of pore to coronal areas was 73.61 % ± 2.31,

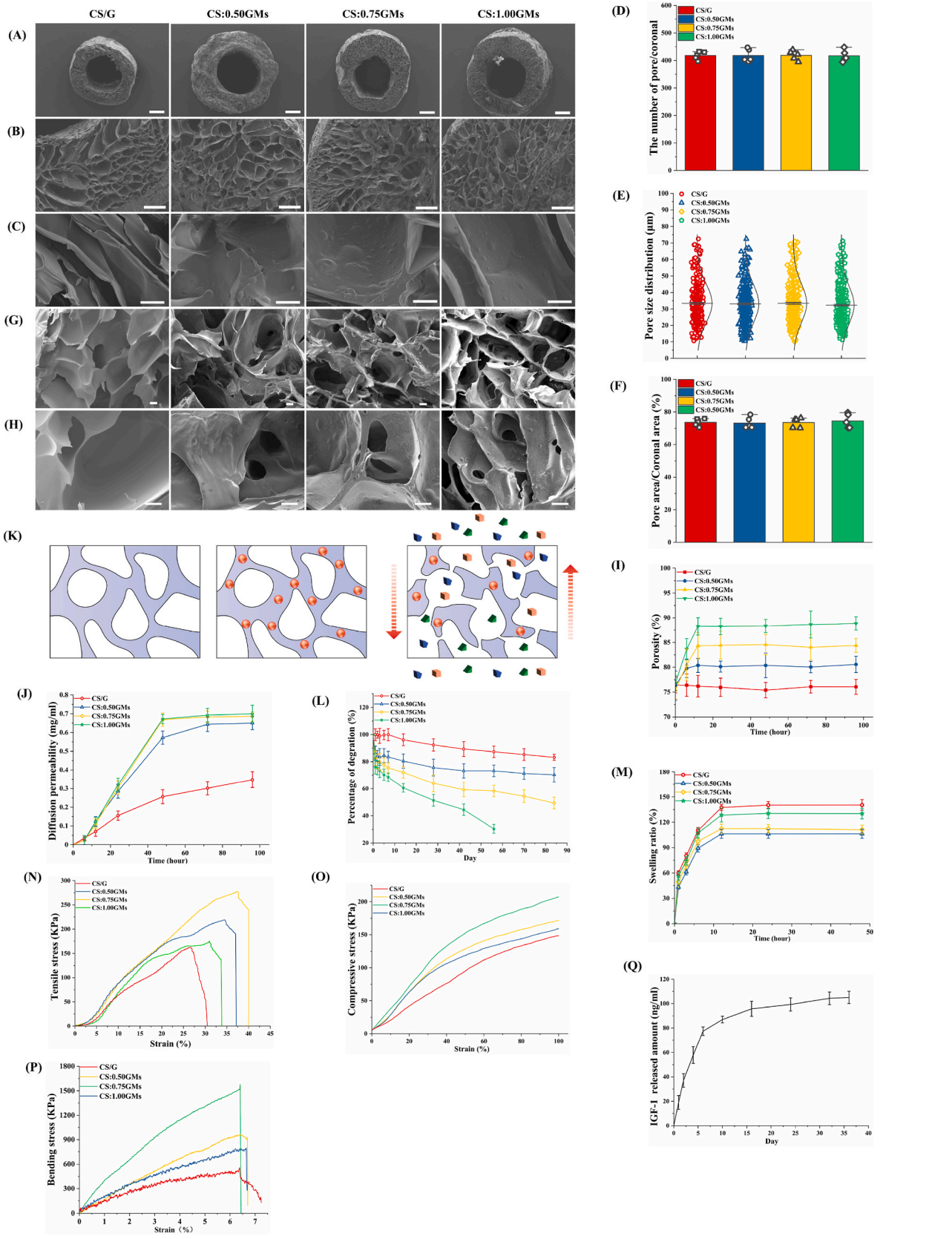

(caption on next page)

Fig. 1. Characterization of the biomimetic ECM GMs-CS nerve conduits. (A, B, and C) SEM images of the honeycomb-like porous structures of nerve conduits prepared by blending CS and GMs at mass ratios of 1:0.50, 1:0.75, and 1:1.00, respectively. Scale bars = 500 μm, 100 μm, and 15 μm. (D, E, and F) Analysis of the pore structure on the coronal plane of the nerve conduits using Image J software, including the number of pores, pore diameter distribution, and pore/coronal plane area ratio. (J, H) SEM images of the 3D interconnected porous network structure of the nerve conduits after immersion in PBS solution for 24 h. Scale bars = 200 μm and 30 μm. (I) Porosity of the nerve conduits after immersion in PBS solution for 6, 12, 24, 48, 72, and 96 h. (J) Permeability kinetics of the sample membranes using starch as a model substance. (K) Schematic diagram illustrating the efficiency of substances exchange inside and outside the nerve conduits facilitated by the 3D interconnected porous network. (L) In vitro degradation rate of the nerve conduits in a 0.5 U/ml collagenase type II solution. (M) Swelling ratio of the nerve conduits after immersion in PBS solution for 1, 3, 6, 12, 24, 48, and 72 h (N, O, P) Sutures tensile mechanical properties, 50 % radial compression performance, and bending strength of nerve conduits with different GM doping ratios. (Q) In vitro release kinetics of IGF-1 detected using an ELISA kit. Data are expressed as mean ± SD. n = 5 per group. $p^*<0.05$.

73.23 % ± 3.15, 73.48 % ± 2.66, and 74.44 % ± 3.90 (Fig. 1F), respectively. The obtained results indicated that the doped multi-functional GMs had no obvious effect on the porous structure of the NGC.

In this study, GMs with diameters ranging from 20 to 80 μm were prepared through emulsification (Supplementary Figs. 1A and B) and cross-linked with a 0.5 wt% genipin solution. Fourier transform infrared spectroscopy (FTIR) analysis (Supplementary Fig. 1C) indicated that genipin interacted with the free amino groups of the gelatine molecules via the Schiff base reaction, thereby promoting self-polymerisation among gelatine molecules. The phenomenon occurred via a two-step process: the primary amines of gelatine polypeptides formed stable intermediates through Michael's addition, followed by nucleophilic substitution with the ester group in genipin to form a secondary amide link [39]. After reacting in a 0.5 wt% genipin solution for 4, 8, 12, and 24 h, the cross-linking degrees (Supplementary Fig. 1E) of GMs were 13.49 ± 2.79, 26.38 ± 3.91, 33.85 ± 4.93, and 68.46 ± 3.80 %, respectively. The corresponding zeta (ζ) potential (Supplementary Fig. 1E) in the PBS solution was −6.33 ± 0.67, −10.37 ± 0.80, −15.74 ± 0.66, and −15.81 ± 0.72, respectively. Thus, the genipin-cross-linked GMs loaded IGF-1, which was positively charged under physiological conditions (PI = 8.2) [36]. Moreover, in vitro degradation studies (Supplementary Fig. 1F) showed that the stability of GMs gradually increased with the degree of cross-linking. Uncross-linked GMs could not exist stably because gelatin, being a water-soluble protein, rapidly dissolved in the PBS solution at 37 °C. GMs cross-linked in a 0.5 wt% genipin solution for 4 h were completely hydrolysed in the PBS solution at 37 °C within 24 h. Whereas, the 24 h cross-linked group remained stable in the PBS solution at 37 °C, with only 29.8 ± 4.2 % hydrolysed over 15 d. GMs with low cross-linking density exhibit loose structure and fewer chemical cross-linking points, making them more prone to hydrolysis and dissolution in the PBS solution, leading to a faster degradation rate [40]. Contrarily, GMs with high cross-linking density exhibit a tighter structure and more cross-linking points, which enhance their chemical stability and physical barrier properties, thereby slowing their degradation rate [41]. Therefore, GMs in NGCs may be assigned different functions based on their surface zeta potentials and hydrolytic stabilities. In this study, inspired by the templating method for preparing porous structures, GMs with a low degree of cross-linking were cross-linked for 4 h (CL-4h) and used as sacrificial templates owing to their rapid dissolution properties for achieving inter-connectivity, openness, and a highly permeable porous network structure. GMs with a high degree of cross-linking were cross-linked for 24h (CL-24h) and loaded with IGF-1 for sustained delivery owing to their high zeta potential and long-term dissolution stability. The CL-4h and CL-24 h GM (loaded or unloaded with IGF-1) were mixed at a mass ratio of 1:1 to form multi-functional GMs.

As shown in Fig. 1G and H, the CS/G conduits exhibited a honeycomb-like porous structure with a smooth wall after being placed in a PBS solution for 24 h at 37 °C. After immersion of the multi-functional GMs-doped NGC in the PBS solution for 24 h, voids appeared in the pore walls between the pores in the CS:0.50 GMs, CS:0.75 GMs, and CS:1.00 GMs groups due to the hydrolysis and dissolution of the sacrificial CL-4h GMs in the PBS solution, resulting in an interconnection between the pore structures. Additionally, in Fig. 1H, the CL-24 h GM with a high degree of cross-linking remained intact in the pore wall, and the pore wall was still rough. The initial porosity (Fig. 1I) of the NGCs in the CS/G, CS: 0.50 GMs, CS: 0.75 GMs, and CS: 1.00 GMs groups was 76.43 % ± 1.60, 76.30 % ± 2.93, 75.37 % ± 1.74, and 76.84 % ± 1.45, respectively, which was consistent with the cross-sectional area of the pore structure. In the CS/G group, the porosity of NGCs in the PBS solution did not change significantly within 96 h, measuring 76.39 % ± 2.25 %, 76.19 % ± 2.15 %, 75.97 % ± 1.85 %, 75.39 % ± 1.54 %, 76.07 % ± 1.26 %, and 76.05 % ± 1.50 %, respectively. In the multi-functional GM doping group, the porosity of the NGCs dynamically increased as CL-4h GMs hydrolysed. Additionally, the maximum porosity of the NGCs increased with the GM mass ratio. The porosity (Fig. 1I) of the CS:0.50 GMs, CS:0.75 GMs, and CS:1.00 GMs groups increased from 76.30 % ± 2.93 %–80.57 % ± 1.64 %, 75.37 % ± 1.74 %–84.38 % ± 1.39 %, and 76.84 % ± 1.45 %–88.85 % ± 1.35 %, respectively. Thus, the results indicated that multi-functional GMs provided NGCs with an interconnected, porous network structure and dynamic porosity. Further, a starch solution was used to simulate the molecular exchange kinetics of bio-signalling molecules across the NGC wall. The permeability efficiency of substances inside and outside the membranes in the CS:0.50 GMs, CS:0.75 GMs, and CS:1.00 GMs groups (Fig. 1J) increased by 1.87 ± 0.04, 1.97 ± 0.02, and 2.01 ± 0.05 times, respectively, compared to the CS/G group. The increase in substance exchange efficiency was due to the establishment of the 3D interconnected porous structure (Fig. 1K).

The results indicated that the freeze-drying method combined with CL-4h GMs as sacrificial templates allowed the construction of a dynamic 3D porous network structure within the NGCs. The 3D interconnected porous structure increased the porosity of the NGCs, enhancing their permeability and efficiency of substance exchange.

3.1.2. Degradation rate, mechanical properties, swelling properties, and kinetics of IGF-1 delivery

The primary objective of evaluating the in vitro degradation, swelling ratio, suture tensile properties, and 50 % radial compression performance of the NGCs was to determine their clinical applicability. As shown in Fig. 1L, the NGCs (CS/G) prepared by blending CS and pure gelatin degraded slowly, which did not match the speed of nerve regeneration and posed challenges for clinical applications. After being immersed in the PBS solution at 37 °C for 3 months, the NGCs degraded by only 16.75 ± 2.25 % (w/w%). However, the degradation rate of the NGCs significantly increased when gelatin was blended with CS in the form of GMs. After 3 months, the degradation rates of CS:0.50 GMs and CS:0.75 GMs were 29.65 % ± 5.35 and 50.65 % ± 4.35, respectively. The CS:1.00 GMs group fragmented after 3 months and failed to maintain a complete tubular structure. From this study, the obtained data demonstrated that, compared with the uniform blending of pure gelatine into CS, blending GMs into CS evidently promoted the degradation rate of the NGCs due to the following reasons. First, when CS was directly blended with pure gelatin, their interaction could have led to gelatin being less soluble and degradable [42]. However, when gelatin was added to the GMs, concentrated hotspots were created for dissolution, consistent with the observed rapid degradation phase of the NGCs within 24 h. Second, the in situ dissolution of CL-4h GMs within the pore wall structure increased the specific surface area of the NGCs, enhancing

their exposure to lysozyme, hydrolase, and collagenase in bodily fluids, thereby accelerating the degradation rate of the composite NGCs. This study demonstrated that the CS:0.75 GMs NGCs maintained their structural integrity after 3 months in a simulated in vivo environment, degrading 50 % of their total mass. The degradation rate aligned with the typical recovery period for PNIs, which was approximately 6 months.

The swelling rates (Fig. 1M) of CS/G, CS:0.50 GMs, CS:0.75 GMs, and CS:1.00 GMs were 140.41 ± 6.31, 106.40 ± 5.37, 111.35 ± 5.30, and 130.26 ± 6.30 %, respectively. CS and gelatin are hydrophilic polymers with high water absorption capacities. Owing to the polypeptide chain structure, gelatin can absorb a significant amount of water, whereas the amino groups in CS can form hydrogen bonds with water molecules [43]. Therefore, the CS and gelatin composite NGCs exhibited a high swelling ratio in water. Additionally, compared to CS/G, NGCs doped with GMs exhibited a lower swelling ratio because, after cross-linking with genipin, gelatin formed a stable cross-linked network between the molecules, significantly reducing the hydrophilicity and swelling capacity of the materials. Cross-linking reduced the gaps between the molecular chains, hindering the infiltration of water molecules. The dense structure of the cross-linked GMs further restricted water entry, reducing the overall water absorption and swelling ratio of the material.

The representative suture tensile properties, 50 % radial compressive performance, and bending strength stress–strain results are presented in Fig. 1N, O, and P. Compared to the CS/G group, the elastic modulus (Table 2) of the NGCs doped with different proportions of GMs increased from 191.30 ± 8.57 to 265.20 ± 13.36, 305.84 ± 11.84, and 214.36 ± 12.94 KPa. Similarly, the elongation at break (Table 2) increased from 54.3 ± 2.1 to 67.5 ± 1.9, 72.1 ± 2.6, and 56.2 ± 2.4 % for CS:0.50 GMs, CS:0.75 GMs, and CS:1.00 GMs, respectively. The compressive modulus (Table 3) increased from 201.39 ± 13.26 KPa in the CS:0.75G group to 307.87 ± 13.74, 347.22 ± 14.57, and 293.98 ± 12.54 KPa for the CS:0.50 GMs, CS:0.75 GMs, and CS:1.00 GMs groups, respectively. Compared to the CS/G group (148.49 ± 12.63 KPa), the compressive strength of the CS:0.50 GMs, CS:0.75 GMs, and CS:1.00 GMs groups increased to 171.89 ± 12.84, 200.51 ± 14.3, and 159.37 ± 13.95 KPa, respectively, attributable to the interfacial integration force between the negatively charged surface of the GMs and the positively charged CS [39]. Similarly, the CS:0.75 GMs group of nerve conduits also exhibited the highest bending modulus and bending strength (Table 4). The GMs and CS formed a composite structure through the interface, transferring the load from the CS matrix to the GM reinforcement. The interfacial bonding force between the CS and GMs dispersed and absorbed crack energy at the interface, preventing crack propagation and reducing stress [44].

The NGCs prepared by mixing CS and multi-functional GMs at a 1:0.75 mass ratio (CS:0.75 GMs) exhibited a suitable degradation rate, water absorption swelling rate, as well as superior suture tensile strength, elongation at break, bending strength and radial compression properties, indicating their potential for clinical application. Therefore, CS:0.75 GMs were selected for subsequent in vitro cytological and in vivo animal studies. ELISA analysis showed that CL-24 h GM could load 662.64 ± 22.7 ng of IGF-1 per mg, with a fixation rate of 82.75 %. The in vitro delivery kinetics studies (Fig. 1Q) of IGF-1-loaded NGCs in the CS:0.75 GMs group showed that IGF-1 was gradually delivered as the high cross-linking degree of GMs slowly degraded.

Table 2
The tensile mechanical properties of CS/G, CS:0.50 GMs, CS:0.75 GMs, and CS:1.00 GMs, tested using a suture thread for stretching, are presented as the mean elastic modulus and breaking elongation for each group.

Samples	Elastic Strength (KPa)	Breaking Elongation (%)
CS/G	191.30 ± 8.57	54.30 ± 2.1
CS:0.50 GMs	265.20 ± 13.36	67.50 ± 1.9
CS:0.75 GMs	305.84 ± 11.84	72.06 ± 2.6
CS:1.00 GMs	214.36 ± 12.94	56.16 ± 2.4

Table 3
The radial pressure resistance properties of the CS/G, CS:0.50 GMs, CS:0.75 GMs, and CS:1.00 GMs groups were determined by measuring the maximum pressure at which the radial displacement of the conduit body reached half of the inner diameter of the conduit.

Samples	Compression modulus (KPa)	Compressive strength (KPa)
CS/G	201.39 ± 13.26	148.49 ± 12.63
CS:0.50 GMs	307.87 ± 13.74	171.89 ± 12.84
CS:0.75 GMs	347.22 ± 14.57	200. 51 ± 14.32
CS:1.00 GMs	293.98 ± 12.54	159.37 ± 13.95

Table 4
Bending performance of CS/G, CS:0.50 GMs, CS:0.75 GMs, and CS:1.00 GMs determined by measuring the bending modulus (MPa) and maximum bending strength (KPa) of the nerve conduits in each group.

Samples	Bending modulus (MPa)	Bending strength (KPa)
CS/G	36.83 ± 2.14	920.35 ± 27.36
CS:0.50 GMs	125.23 ± 2.94	2785.57 ± 38.86
CS:0.75 GMs	64.82 ± 4.24	1620.58 ± 46.68
CS:1.00 GMs	39.70 ± 3.20	992.45 ± 28.48

3.2. Promotion of differentiation of SCs and PC12 cells by interconnected porous networks and sustained IGF-1 delivery

Further, we investigated the effects of the interconnected porous network structure and sustained IGF-1 delivery on the in vitro functions of the RSC96 and PC12 cells. An NGC with a closed, non-connected porous structure prepared from CS and pure gelatin was used as a control group (CS/G). NGCs prepared by blending CS with multi-functional GMs (loaded or unloaded with IGF-1) were used as NGCs with a 3D interconnected porous network structure (CS/GMs) and those with a 3D interconnected porous network structure and sustained IGF-1 delivery (CS/GMs@IGF-1).

The cell viability after 24 and 72 h of extraction of CS/G NGCs was 92.1 ± 4.1 and 90.1 ± 2.9 %, respectively, indicating that CS/G exhibited low potential toxicity (Fig. 2A). The multi-functional GMs imparted good cytocompatibility to the NGCs, with cell viability after 24 and 72 h of extraction of 96.1 ± 3.6 and 97.2 ± 3.2 %, respectively. The result was attributed to the high bioactivity of the water-soluble proteins leached from the hydrolysis and dissolution of the CL-4h GMs. The cell viability of the CS/GMs@IGF-1 group was significantly higher than that of the other groups. Additionally, the cell viability after 72 h of extraction (106.4 % ± 2.3 %) was significantly enhanced compared to that after 24 h of extraction (98.9 % ± 4.2 %), attributed to the delivery of IGF-1. Live/dead cell staining using AM-PI (Supplementary Fig. 2) confirmed the same trend: the CS/GMs@IGF-1 group exhibited the strongest and weakest green (live cells) and red (dead cells) fluorescence intensities, respectively. The extracted liquid and AM-PI staining results demonstrated that NGCs doped with GMs and loaded with IGF-1 exhibited excellent cytocompatibility, supporting the survival of RSC96 cells within the NGCs.

The proliferation of RSC96 cells on NGCs was assessed using the CCK-8 assay after 1, 3, and 7 d of culture, as shown in Fig. 2B. After 1 d of culture, the OD values of the CS/GMs and CS/G groups did not show significant differences because the CL-4h GMs were still in the process of dissolution, the interconnected pore structure network was not fully established, and the difference in the 3D porous morphology between the two groups was not significant. On days 3 and 7, after the in situ leaching of the CL-4h GMs to form a 3D interconnected porous network structure, the OD value of the CS/GMs group was significantly higher than that of the CS/G, indicating that the interconnectivity of the porous structure had a significant effect on the proliferation of RSC96 cells.

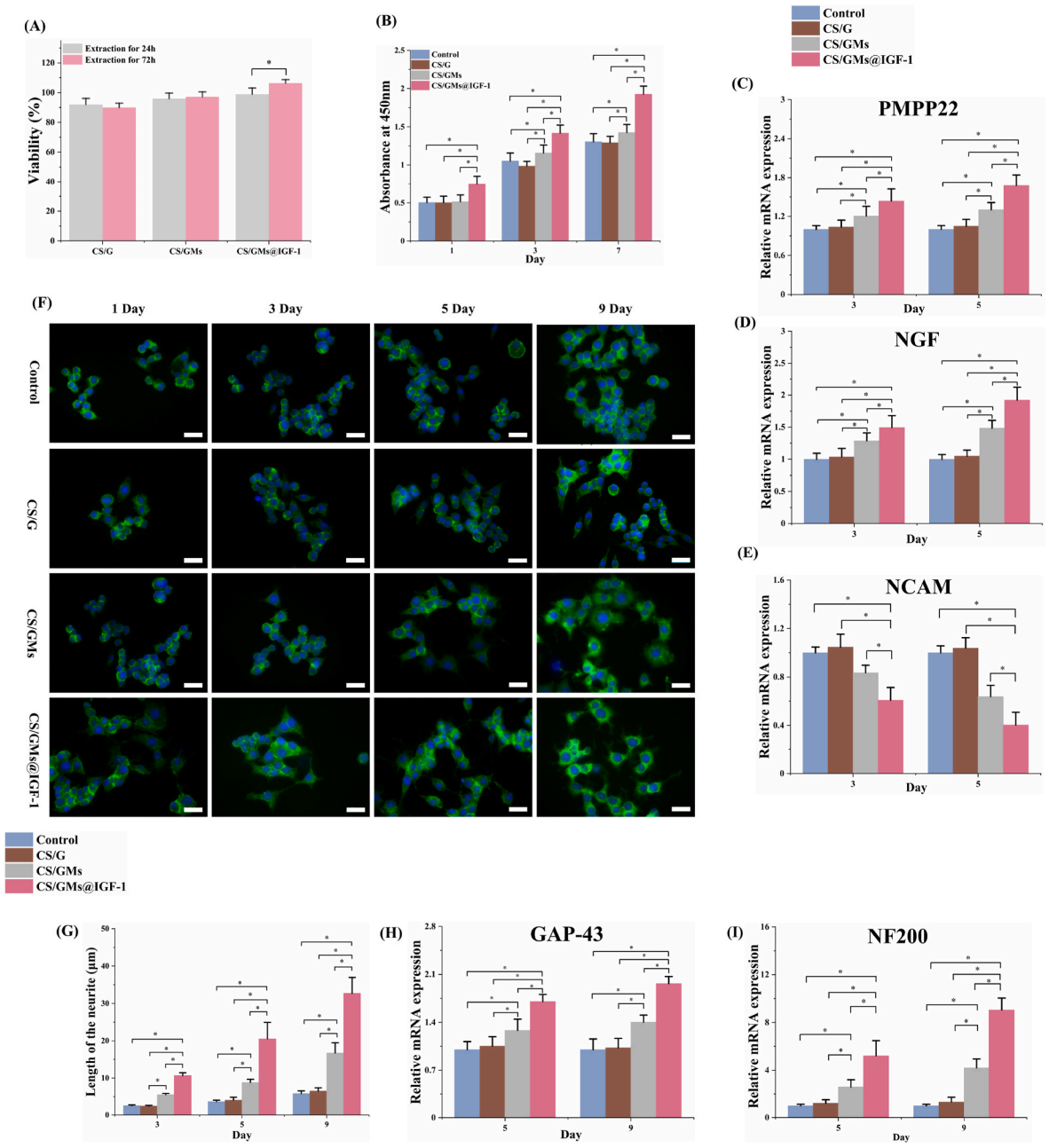

Fig. 2. 3D interconnected porous network sustained IGF-1 delivery nerve conduits to promote SC survival, proliferation, remyelination, and axonal growth. (A) Effect of nerve conduit extracts on RSC96 cell viability after 24 and 72 h. (B) Cell viability of RSC96 cells cultured on different sample membranes for 1, 3, and 7 d, assessed using the CCK-8 assay. (C, D, E) Relative expression levels of myelination-related genes in RSC96 cells evaluated by qRT-PCR, examining the impact of the 3D interconnected porous network and sustained IGF-1 delivery. (F) Representative IF images showing the effect of the 3D interconnected porous network and sustained IGF-1 delivery on PC12 cell neurite outgrowth at 1, 3, 5, and 9 d. Scale bars = 50 μm. (G) Statistical analysis of neurite length in PC12 cells cultured on different samples for 1, 3, 5, and 9 d, conducted using Image J. (H, I) Relative expression levels of axonal growth-related genes in PC12 cells evaluated by qRT-PCR, analyzing the impact of the 3D interconnected porous network and sustained IGF-1 delivery. Data are expressed as mean ± SD. n = 3 per group. $p^*<0.05$.

Moreover, after 1, 3, and 7 d of culture, the OD value of CS/GMs@IGF-1 was significantly higher than those of the CS/G and CS/GMs groups, indicating that IGF-1 significantly promoted the proliferation of RSC96 cells.

Furthermore, the potential for myelination in RSC96 cells at 3 and 5 days was measured by qRT-PCR to detect the transcription levels of myelination-related markers (PMP22, NGF, and NCAM), as shown in Fig. 2C, D, and E. Compared with the CS/GMs group demonstrated significantly upregulated PMP22 and NGF gene expression and down-regulated NCAM transcription levels in the RSC96 cells after incubation for 3 and 5 d. After loading IGF-1 with CL-24 h GM, the increase in PMP22 and NGF gene expression and the decrease in NCAM gene expression in the CS/GMs@IGF-1 group were more significant than those in the CS/G and CS/GMs groups, indicating that sustained delivery of IGF-1 promoted the differentiation of RSC96 cells from an unmyelinated to myelinated state.

Undifferentiated PC12 cells were used to investigate the effects of biomimetic ECM NGCs with 3D interconnected porous networks and sustained IGF-1 delivery on neurite outgrowth. As shown in Fig. 2F, PC12 cells were attached to each grouped sample after 1 d of culture, showing a small and round cell morphology with no significant difference, and the length of neurites could not be counted because they were

not yet grown. After 3 d of cultivation, the formation trends of neural axons in each group exhibited significant differences. Compared with the control and CS/G groups, in which cellular morphology showed a disc-shaped unstretched state, the PC12 cells in the CS/GMs group were stretched in a flat state, and some cells were observed to exhibit short protrusions. The PC12 cells in the CS/GMs@IGF-1 group spread more evidently; some cells extended more than one protrusions, and the protrusion was longer. The protruding lengths of PC12 cells (Fig. 2G) in 3 d of the control, CS/G, CS/GMs, and CS/GMs@IGF-1 groups were 2.6 ± 0.2, 2.4 ± 0.2, 5.5 ± 0.3, and 10.6 ± 0.7 μm, respectively. With the

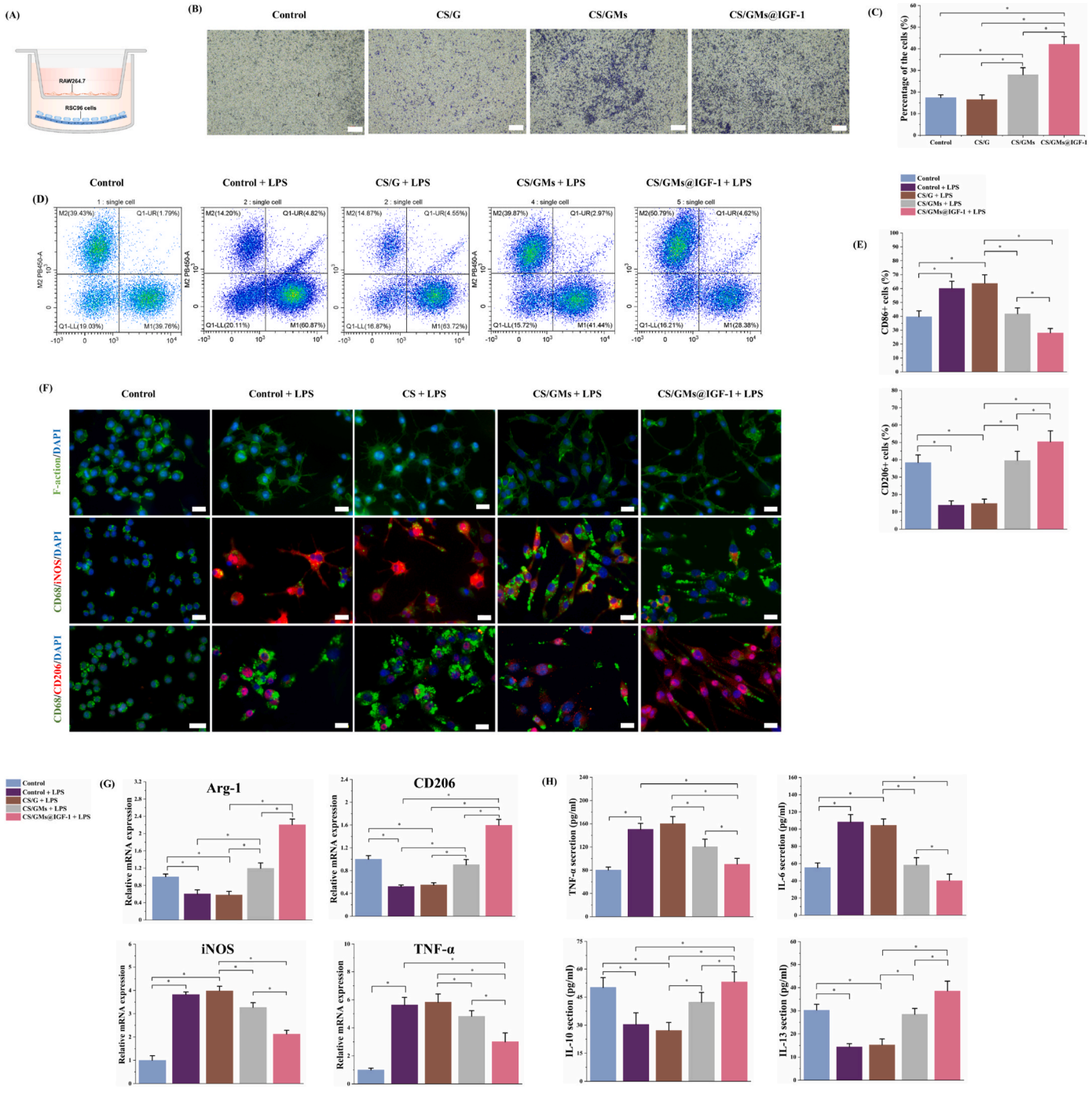

Fig. 3. Effects of the biomimetic ECM nerve conduit on macrophage recruitment and polarisation. (A) Schematic diagram illustrating the impact of activated SCs on macrophage recruitment in a Transwell co-culture system. (B) Representative images showing the effect of RSC96 cells cultured on different substrates on the recruitment of RAW264.7 cells. RAW264.7 cells were stained purple with crystal violet. Scale bars = 200 μm. (C) Quantitative analysis of recruited RAW264.7 cells. (D) Flow cytometry analysis of the impact of the 3D interconnected porous network and sustained IGF-1 delivery on the immunephenotype polarisation of RAW264.7 cells under LPS-stimulated inflammatory conditions. (E) Quantitative analysis of CD86-positive (M1) and CD206-positive (M2) RAW264.7 cells. (F) F-actin staining with FITC-labeled phalloidin to observe the morphology of RAW264.7 cells cultured under different substrate conditions. Immunofluorescence detection of CD68 (M0, pan-macrophage, green), iNOS (M1, pro-inflammatory, red), and CD206 (M2, anti-inflammatory, red) expression in RAW264.7 cells. Nuclei were stained blue with DAPI. Scale bars = 20 μm. (G) qRT-PCR analysis of the transcription levels of macrophage polarisation-related genes (iNOS, TNF-α, CD206, Arg-1) in RAW264.7 cells cultured on different substrates for 3 d. (H) ELISA analysis of the secretion levels of anti-inflammatory cytokines (IL-10 and IL-13) and pro-inflammatory cytokines (TNF-α and IL-6). Data are expressed as mean ± SD. n = 3 per group. $p^*<0.05$.

extension of the cultivation period, differentiation of PC12 cells became more pronounced on days 5 and 9. Some of the PC12 cells in the control and CS/G groups were still round in shape, but only some began to flatten and form short protrusions. However, in the CS/GM group, more cells differentiated into neuron-like cells, cell size began to increase, neurites began to grow, and cells formed a bipolar morphology with two main protrusions by 9 d. With the extension of culture time, the extension area of PC12 cells in the CS/GMs@IGF-1 group continued to increase, the amount of cytoplasm increased, and the neurites continued to extend and branch, forming a complex network structure similar to the morphology of neurones. The lengths of neurite outgrowth in control, CS, CS/GM, and CS/GM@IGF-1 cells were 5.8 ± 0.7, 6.5 ± 0.9, 16.7 ± 2.8, and 32.7 ± 4.3 μm on the 9 d, respectively.

Further, the expression of GAP-43 and NF-200 in PC12 cells was examined using qRT-PCR (Fig. 2H and I). Consistent with the results of IF staining, GAP-43 and NF200 were significantly upregulated in the interconnected porous network structure group (CS/GMs) compared to those in the CS/G group. Moreover, CS/GMs@IGF-1 exhibited the highest expression of GAP-43 and NF200 among all the groups. Thus, the interconnected open porous network structure provided a supportive microenvironment for PC12 cells relative to the closed porous structure. The effect was further enhanced by the addition of IGF-1, which accelerated neurite outgrowth and branching.

The obtained results suggested that biomimetic ECM NGCs with an 3D interconnected porous network and sustained IGF-1 delivery promoted the survival, proliferation, and remyelination of SCs, along with axon growth after PNI, thereby providing a supportive microenvironment for nerve regeneration.

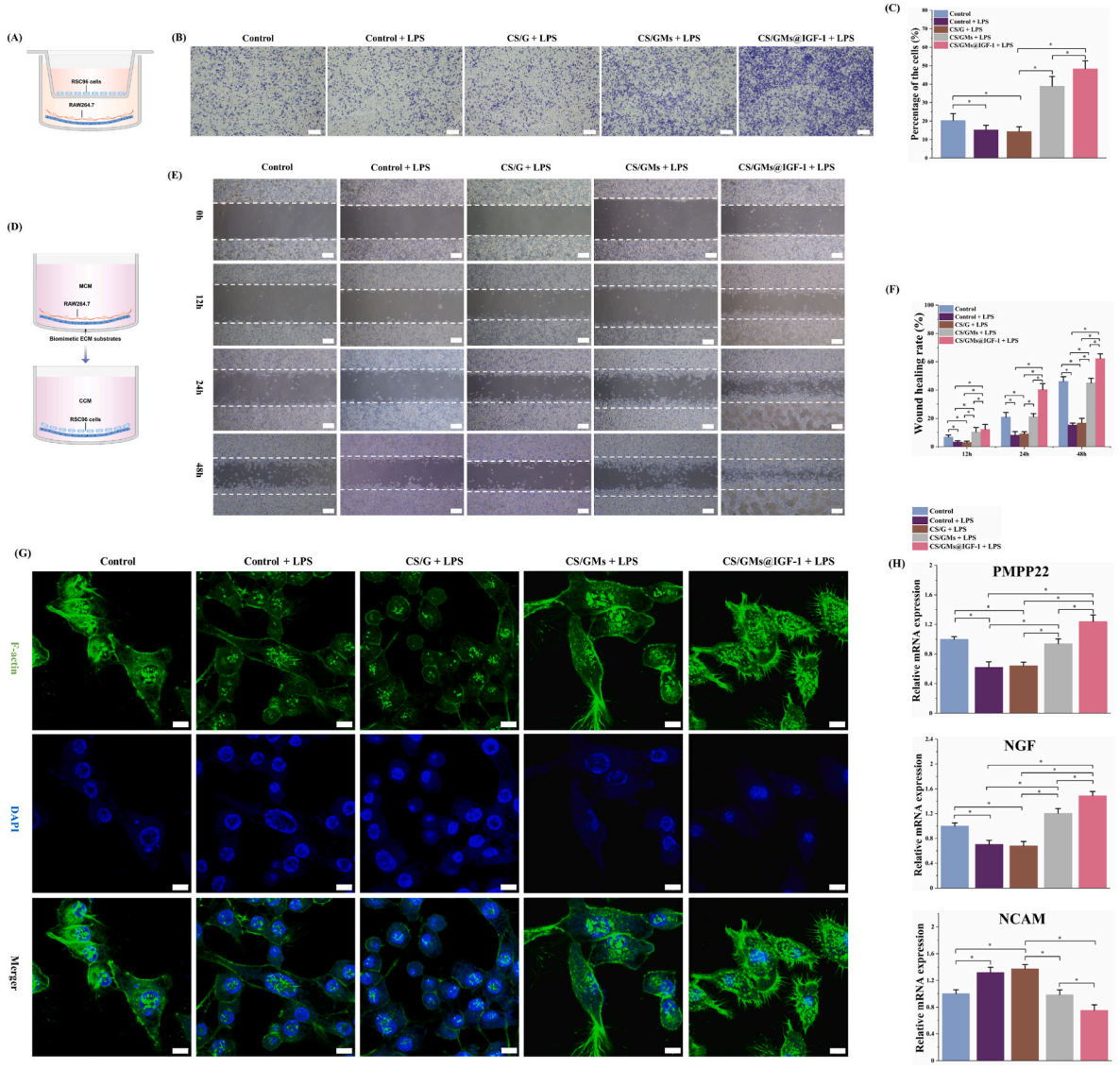

Fig. 4. Effects of the 3D interconnected porous network with sustained IGF-1 delivery in biomimetic ECM nerve conduits on SC migration, actin filament elongation, and remyelination through the regulation of macrophage phenotype polarisation. (A) Schematic diagram illustrating the impact of macrophage phenotype polarisation on Schwann cell migration using a Transwell co-culture system. (B) Representative images of longitudinal migration of RSC96 cells influenced by RAW264.7 cells cultured on different substrates. RSC96 cells were stained purple with crystal violet. Scale bars = 200 μm. (C) Quantitative analysis of longitudinal migration of RSC96 cells. (D) Schematic diagram illustrating the effect of macrophage-conditioned medium on the lateral migration of RSC96 cells. (E) Representative images of lateral migration of RSC96 cells at 12, 24, and 48 h in a wound healing assay, influenced by macrophage-conditioned medium from different substrates. Scale bars = 200 μm. (F) Quantitative analysis of wound healing rates. (G) Representative IF images showing actin filament elongation in RSC96 cells cultured for 24 h with macrophage-conditioned medium from different substrates. Scale bars = 20 μm. (H) qRT-PCR analysis of the relative expression levels of remyelination-related genes (PMP22, NGF, NCAM) in RSC96 cells cultured for 3 d with macrophage-conditioned medium from different substrates. Data are expressed as mean ± SD. n = 3 per group. $p^*<0.05$.

3.3. Promotion of the recruitment and polarisation of macrophages in vitro by interconnected porous networks and sustained IGF-1 delivery

As the recruitment of macrophages after PNI was primarily regulated by cytokines secreted by activated SCs, RSC96 cells were cultured in an 3D interconnected porous network with sustained IGF-1 delivery matrices in the lower chamber of the Transwell co-culture system (Fig. 3A) to simulate the recruitment of macrophages. Crystal violet staining and quantitative analysis (Fig. 3B and C) revealed that macrophage recruitment was significantly enhanced in the RSC96 cells cultured on CS/GMs compared with those cultured on CS/G because the 3D interconnected porous network structure promotes the early activation of SCs, which in turn facilitates the recruitment of macrophages. Furthermore, the number of macrophages migrating towards the CS/GMs@IGF-1 group was the highest among all groups, indicating that the biomimetic ECM NGCs with the 3D interconnected porous network structure and sustained IGF-1 delivery effectively achieved early macrophage recruitment.

Subsequently, flow cytometry, IF staining, qRT-PCR, and ELISA were used to explore the immunophenotypic polarisation of macrophages cultured on different substrates. The RAW264.7 cells cultured on blank plates (with or without LPS) were used as controls. LPS (1 μg/mL) was applied to macrophages to simulate inflammatory injury under nerve damage. CD86, iNOS, and TNF-α were considered biomarkers of M1 macrophages, while CD206 and Arg-1 were regarded as M2 macrophage markers. Flow cytometry analysis (Fig. 3D) showed that LPS significantly stimulated the transformation of macrophages to the M1 type compared with the control group, as the ratio of CD86-positive macrophages (Fig. 3E) in the control + LPS and CS/G + LPS groups was 60.1 ± 3.7 and 63.2 ± 5.4 %, respectively. The 3D interconnected porous network significantly reversed the polarisation trend of macrophages. After 3 d of culture in the CS/GMs + LPS group, the CD86-positive macrophage ratio was 40.2 ± 4.2 %, while CD206-positive macrophages were 39.87 ± 5.3 %. After IGF-1 loading, the trend of promoting macrophages to the M2 phenotype was more pronounced, as the ratio of CD68-positive macrophages and CD206-positive macrophages in the CS/GMs@IGF-1 + LPS group was 28.4 ± 3.1 and 50.8 ± 6.3 %, respectively. Morphological alterations in macrophages cultured on various substrates were visualised by staining for cytoskeletal proteins (F-actin). As shown in Fig. 3F, macrophages in the control + LPS and CS/G + LPS groups changed from small and round in the resting state to pancake-like after 3 d of LPS stimulation, accompanied by an increase in the cell spreading area. However, the macrophages cultured in the interconnected porous network structure groups (CS/GMs) had a smaller area of cell extension and formed fewer cellular pseudopodia, with some cells taking on an oval or fusiform shape, which was characteristic of M2 phenotype macrophages. In the CS/GMs@IGF-1 + LPS group, most macrophages exhibited an elongated oval or spindle shape with smaller cell extension areas and fewer pseudopodia, which were morphological characteristics of macrophages polarising towards the M2 immune phenotype. The qRT-PCR (Fig. 3G) test demonstrated that the CS/GMs group, with its interconnected porous network structure, downregulated the relative levels of iNOS and TNF-α mRNA transcripts in macrophages and upregulated the relative levels of Arg-1 and CD206 mRNA transcripts compared to the CS/G group. Moreover, the CS/GMs@IGF-1 + LPS group showed the most significant increase in the relative gene expression of M2 macrophages and a reduction in the relative gene expression of M1 macrophages. ELISA (Fig. 3H) was used to examine the secretion of inflammation-related factors (IL-10, IL-6, IL-13 and TNF-α) after 3 d of culture on different substrate membranes. The CS/GMs + LPS group significantly reduced the secretion of IL-6 and TNF-α and enhanced the secretion of IL-10 and IL-13 compared to the CS/G + LPS and control + LPS groups. After loading with IGF-1, the CS/GMs@IGF-1 + LPS group showed a more significant decrease in IL-6 and TNF-α secretion and an increase in IL-10 and IL-13 secretion by macrophages.

Thus, the biomimetic ECM NGC with the 3D interconnected porous network and sustained IGF-1 delivery favoured macrophage polarisation towards pro-healing M2 phenotypes, characterised by an elongated morphology and increased expression of anti-inflammatory genes and cytokines.

3.4. Promotion of migration, pseudopod extension, and remyelination of RSC96 cells in vitro by activated macrophages

As shown in Fig. 4A, a transwell chamber assay was used to investigate the effect of the 3D interconnected porous network and sustained IGF-1 delivery on the longitudinal migration of SCs by promoting macrophage phenotype polarisation. Crystal violet staining and quantitative analysis (Fig. 4B and C) showed that the formation of M1 macrophages stimulated by LPS was not conducive to the longitudinal migration of SCs, as the longitudinal migration of RSC96 in the control + LPS and CS/G + LPS groups decreased. However, the visual results and corresponding quantitative data showed a significant increase in the longitudinal migration of SCs in the CS/GMs + LPS group, which was attributed to the 3D interconnected porous network promoting macrophage polarisation towards the M2 phenotype. Moreover, the longitudinal migration of SCs in the CS/GMs@IGF-1 + LPS group was the most significant compared to that in the other groups, as this group promoted the transformation of macrophages to the M2 phenotype most significantly, as previously verified. Macrophage-conditioned medium (MCM) obtained from the culture supernatants of macrophages exposed to different substrates (control, control + LPS, CS/G + LPS, CS/GM + LPS, and CS/GMs@IGF-1 + LPS groups) was used to cultivate the RSC96 cells, as illustrated in Fig. 4D. A wound scratch assay to assess horizontal migration of RSC96 cells under MCM stimulation showed that the healing rates in the CS/GMs MCM exposure group were significantly improved in inflammatory environments at three-time intervals (Fig. 4E), which was similar to the results of the control group. Comparatively, the CS/G + LPS and LPS alone groups showed less scratch gap closure (the healing rates at 48 h (15.4 ± 1.2 and 16.8 ± 3.3 %, respectively). The healing rate of the CS/GMs@IGF-1 group was the highest among all the groups (Fig. 4F), while those at 12, 24, and 48 h were 12.3 ± 3.5, 40.4 ± 4.2, and 62.3 ± 3.2 %, respectively. Such significant differences in the transwell assay and wound healing experiments implied that the interconnected porous network structure and sustained delivery of IGF-1 promoted the migration ability of SCs by regulating the immunophenotype of macrophages to the M2 type.

As shown in Fig. 4G, the RSC96 cells cultivated in the control + LPS and CS/G + LPS MCM groups remained small, round, or spindle-shaped after 24 h of culture, and almost no pseudopodia formation was observed. Comparatively, the RSC96 cells in the control group showed a flat shape, a relatively large cell volume, and a few pseudopodia formations. Thus, the M1-phenotype macrophage-mediated inflammatory microenvironment, in which non-interconnected porous structures were located, was not conducive to the extension of the RSC96 cell cytoskeleton and the growth of pseudopodia. Contrarily, the RSC96 cells cultured in the CS/GMs + LPS group of interconnected porous network-regulated M2-phenotype MCM extended into a flat shape, with the formation of membrane folds and the beginning of processes at the cell edge, which was the preliminary stage of pseudopodia formation. Moreover, the RSC96 cells incubated with CS/GMs@IGF-1 + LPS exhibited a disc-shaped flat cell morphology with an increased attachment area, and membrane folds and processes at the cell edge gradually extended and fused to form pseudopodia due to the biomimetic ECM NGC with the 3D interconnected porous network and sustained delivery of IGF-1, promoting the extension of the RSC96 cell cytoskeleton and the growth of pseudopodia by regulating the polarisation of macrophages to the M2 phenotype.

The effect of macrophage immunophenotypic polarisation on SC remyelination when cultured on different sample substrates was further investigated. Compared to the control group, the expression of PMP22

and NGF was lower, whereas the expression of NCAM was higher in the RSC96 cells cultured in the control + LPS and CS/G + LPS MCM exposure groups. Thus, the immune microenvironment mediated by M1 macrophages in the closed, non-interconnected porous structure was not conducive to the remyelination of the RSC96 cells (Fig. 4H). The MCM of the CS/GM + LPS exposure group could reverse the relative expression of myelinating genes in the RSC96 cells, such that the expressions of PMPP22 and NGF increased while that of NCAM decreased, owing to the regulation of macrophages to the M2 phenotype by the interconnected porous network. Moreover, in the RSC96 cells cultured in CS/GMs@IGF-1 + LPS MCM, the relative expression of the myelin genes PMP22 and NGF was upregulated, while NCAM was downregulated, most significantly compared to the other groups. The effect was due to IGF-1 delivery and the 3D interconnected porous network structure, which significantly regulated the immune microenvironment by polarising macrophages towards the M2 phenotype, thereby significantly promoting SC remyelination.

The obtained data indicated that the biomimetic ECM NGC with 3D interconnected porous networks and sustained IGF-1 delivery regulated the polarisation of macrophages to the M2 immune phenotype. The immune microenvironment of activated MCM promoted the migration, spread, maturation, and remyelination of SCs.

3.5. Promotion of SC proliferation, macrophage recruitment, and polarisation, by biomimetic ECM NGCs during the early grafting period

The effects of the 3D interconnected porous network and sustained IGF-1 delivery on macrophage recruitment, polarisation, and subsequent peripheral nerve regeneration were assessed at 1 and 2 w postoperatively in a 10 mm rat sciatic nerve defect model. As shown in Fig. 5A, the total number of pan-macrophages (M0), pro-inflammatory macrophages (M1), pro-healing macrophages (M2), and SCs was identified by immunofluorescence staining for CD68, iNOS, CD206, and S100β, respectively, in a 2 mm transverse section proximal to the NGC. The results (Fig. 5B and C) showed no significant difference in the expression of S100β among all groups 1 w post-implantation. However, at 2 w post-implantation, the S100β IF intensity in the CS/GMs nerve conduits was significantly higher than that in the CS/G group, indicating that the 3D interconnected porous structure in the nerve conduits promoted early SC remyelination following implantation. After loading with IGF-1, the CS/GMs@IGF-1 group exhibited the highest S100β IF intensity among all groups, indicating that the sustained delivery of IGF-1 further enhanced the early promotion of SC myelination.

Subsequently, the number of macrophages infiltrating the NGCs and the polarisation of their immune phenotypes at 1 and 2 w post-implantation were investigated. The IF intensities of the $CD68^{+}$ and CD206+ M2-like phenotypes in the CS/GMs group were significantly higher at 1 and 2 w post-implantation than those in the CS/G group. Statistical analysis of the five IF images showed the number of M0 macrophages (Fig. 5D) in the CS/GMs group was 105 ± 7 and 185 ± 7 per field at 1 and 2 w, respectively, which was significantly higher than 41 ± 7 and 75 ± 7 per field in the CS/G group. Statistical analysis of iNOS and CD206+ markers showed that the proportion of M2/M1 macrophages (Fig. 5E) was significantly higher in the CS/GMs group (1.15 ± 0.13, 1.46 ± 0.21) than that in the CS/G group (0.94 ± 0.09, 1.03 ± 0.25) at 1 and 2 w. Thus, compared to the closed, non-interconnected porous structure, the interconnected porous network significantly enhanced macrophage recruitment and promoted the polarisation of infiltrating macrophages towards the M2 phenotype. After loading IGF-1, the CS/GMs@IGF-1 group NGCs exhibited increased numbers of infiltrating M0 macrophages (175 ± 8, 314 ± 6), CD206+ IF intensity, and M2/M1 macrophage ratios (1.25 ± 0.21, 2.94 ± 0.33) at 1 and 2 w post-implantation compared to the CS/GMs group NGC. Thus, the sustained delivery of IGF-1 further increased the number of infiltrating macrophages and regulated their polarisation towards the M2 phenotype.

Therefore, the biomimetic ECM NGC with a 3D interconnected porous network and sustained IGF-1 delivery promoted SC maturation by rapidly recruiting macrophages and polarising them towards the pro-healing (M2) phenotype.

3.6. Promotion of axonal regeneration and myelination during long-term implantation by biomimetic ECM NGCs

IF, TEM, and TB staining were used to further investigate the effects of interconnected porous network structures and sustained IGF-1 delivery on axonal regeneration and remyelination of peripheral nerves. Nerve graft samples were collected 12 w after the nerve conduits were implanted in vivo, and cross-sections of the regenerated nerve at a distance of 2 mm were observed. TB-stained images (Fig. 6A) revealed that uniform myelinated nerve fibres were successfully regenerated in all groups at 12 w postoperatively. Quantitative analysis (Fig. 6B) showed that the autograft group (11210 ± 780 nerve/mm^2) had the highest number of myelinated nerve fibres among all groups. The number of myelinated nerve fibres in the CS/GMs@IGF-1 group (10920 ± 739 nerve/mm^2) was similar to that in autografts and significantly higher than that in the CS/G and CS/GMs groups. The density of myelinated nerve fibres in the CS/GMs group (6320 ± 638 nerve/mm^2) was significantly increased compared to the CS/G group (8090 ± 839 nerve/mm^2). The results of TB staining showed that the interconnected porous network and IGF-1 delivery to the NGCs promoted the regeneration of axons during peripheral nerve repair.

The morphology and myelin sheath thickness of the regenerated nerve were observed using TEM to determine the electrical conduction velocity, maturity, and remyelination of the regenerated nerve. The newly regenerated nerve fibres in the CS/GMs@IGF-1 group and autograft group were mainly regular oval shapes, with the diameter of regenerated nerve fibres (Fig. 6C) being 3.80 ± 0.19 and 3.5 ± 0.21 μm, and the myelin sheath thickness (Fig. 6D) being 1.25 ± 0.07 and 1.19 ± 0.09 μm, respectively. The diameter of the nerve fibres (3.05 ± 0.23 μm) and the thickness of the myelin sheath (0.95 ± 0.23 μm) in the CS/GMs group were lower than those in the CS/GMs@IGF-1 group but higher than those in the CS/G group (nerve fibre diameter: 2.58 ± 0.19 μm, myelin sheath thickness: 0.60 ± 0.08 μm). Thus, the interconnected porous network promoted myelin regeneration in the regenerated axons, and sustained delivery of IGF-1 further enhanced the promoting effect. Subsequently, the *g*-ratio of the regenerated myelinated fibres, defined as the ratio of the inner diameter to the outer diameter of the neurites, indicating the optimal function and structure of neural myelination, was calculated. As shown in Fig. 6E, the *g*-ratio distribution trend of the CS/GMs@IGF-1 group was comparable to that of autografts, and the value of *g*-ratio gradually increased following the order: Autograft (0.63 ± 0.04) < CS/GMs@IGF-1 (0.65 ± 0.05) < CS/GMs (0.67 ± 0.07) < CS/G (0.71 ± 0.06). Previous studies have reported that the *g*-ratio of healthy sciatic nerves is approximately 0.6 [45]. By constructing an interconnected porous network and loading IGF-1 into the nerve conduit, the *g*-ratio value of regenerated nerves in the CS/GMs@IGF-1 group was reduced to the normal range, and axon diameters became larger, close to those of autografts. Additionally, the fitting curve (Fig. 6F) of the *g*-ratios in each group revealed that the myelin degree of the regenerative nerves in the CS/GMs@IGF-1 group was closest to that in the autograft group. Notably, axons in the CS/G group, mostly with small diameters, had higher *g*-ratios than those in the CS/GMs group, indicating that the potential for remyelination of regenerated axons in the non-interconnected porous structure group was lower. Contrarily, the fitting curves of the CS/GMs and CS/GMs@IGF-1 groups cut across each other, indicating that the CS/GMs group had more myelinated nerves with small diameters and a low *g*-ratio, which exhibited the potential for remyelination.

IF staining for axonal protein NF200 and myelination-specific protein S100β was performed to further evaluate axonal regeneration and SC remyelination (Fig. 6G), respectively. Compared with the closed non-

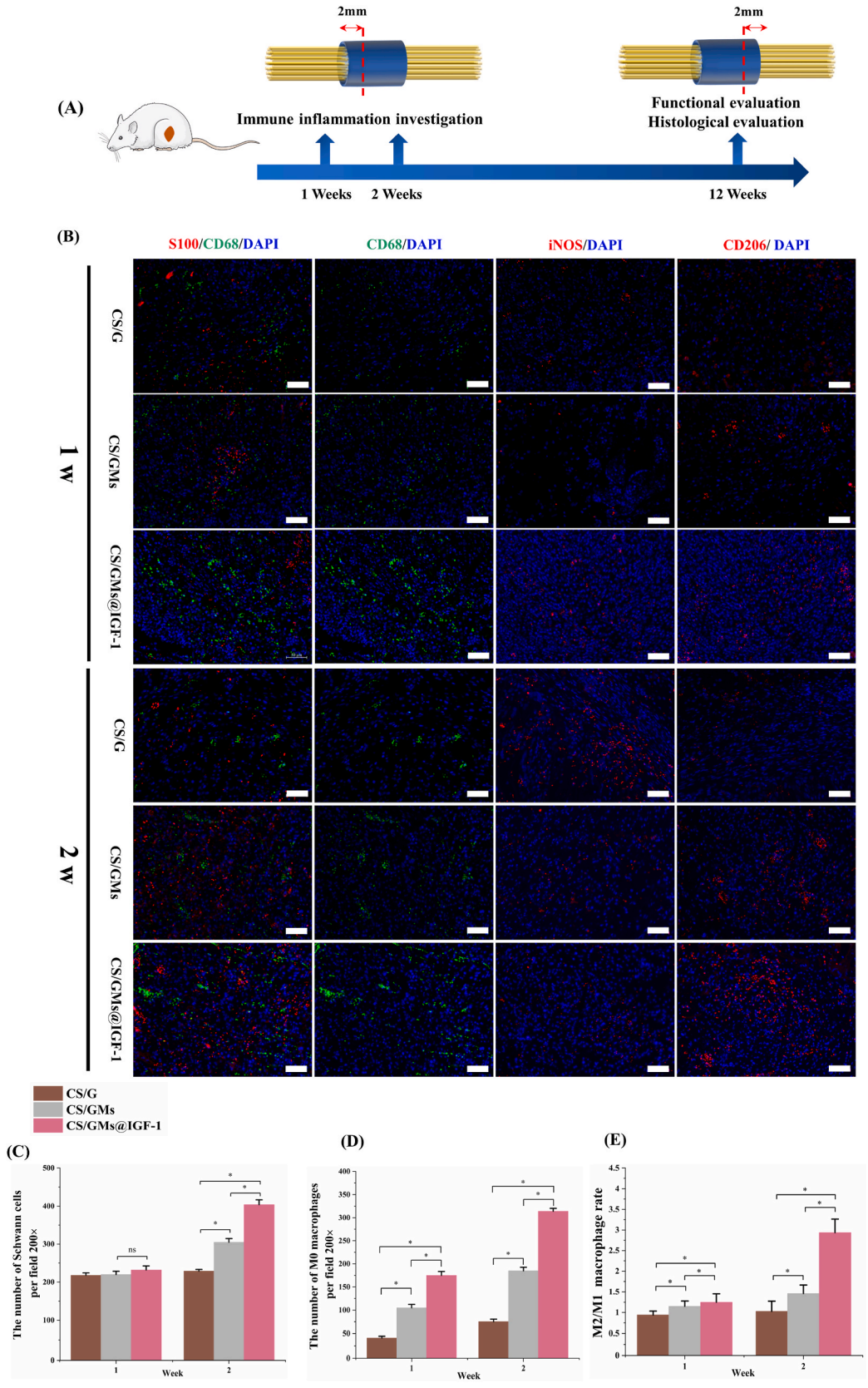

Fig. 5. Relationship between macrophage polarisation and SCs in vivo at 1 and 2 w post-implantation. (A) Schematic diagram of the in vivo analysis of a 10 mm sciatic nerve defect model in rats. (B) Immunostaining for S100β (SCs, red), CD68 (M0, pan-macrophage, green), iNOS (M1, pro-inflammatory, red), and CD206 (M2, anti-inflammatory, red) at 1 and 2 w post-nerve conduit implantation. Scale bars = 100 μm. (C, D, E) Quantification of the number of regenerated SCs, infiltrated M0 macrophages in the nerve conduit, and the M2/M1 macrophage ratio. Data are expressed as mean ± SD. n = 11 per group. $p^*<0.05$. Ns, no significance.

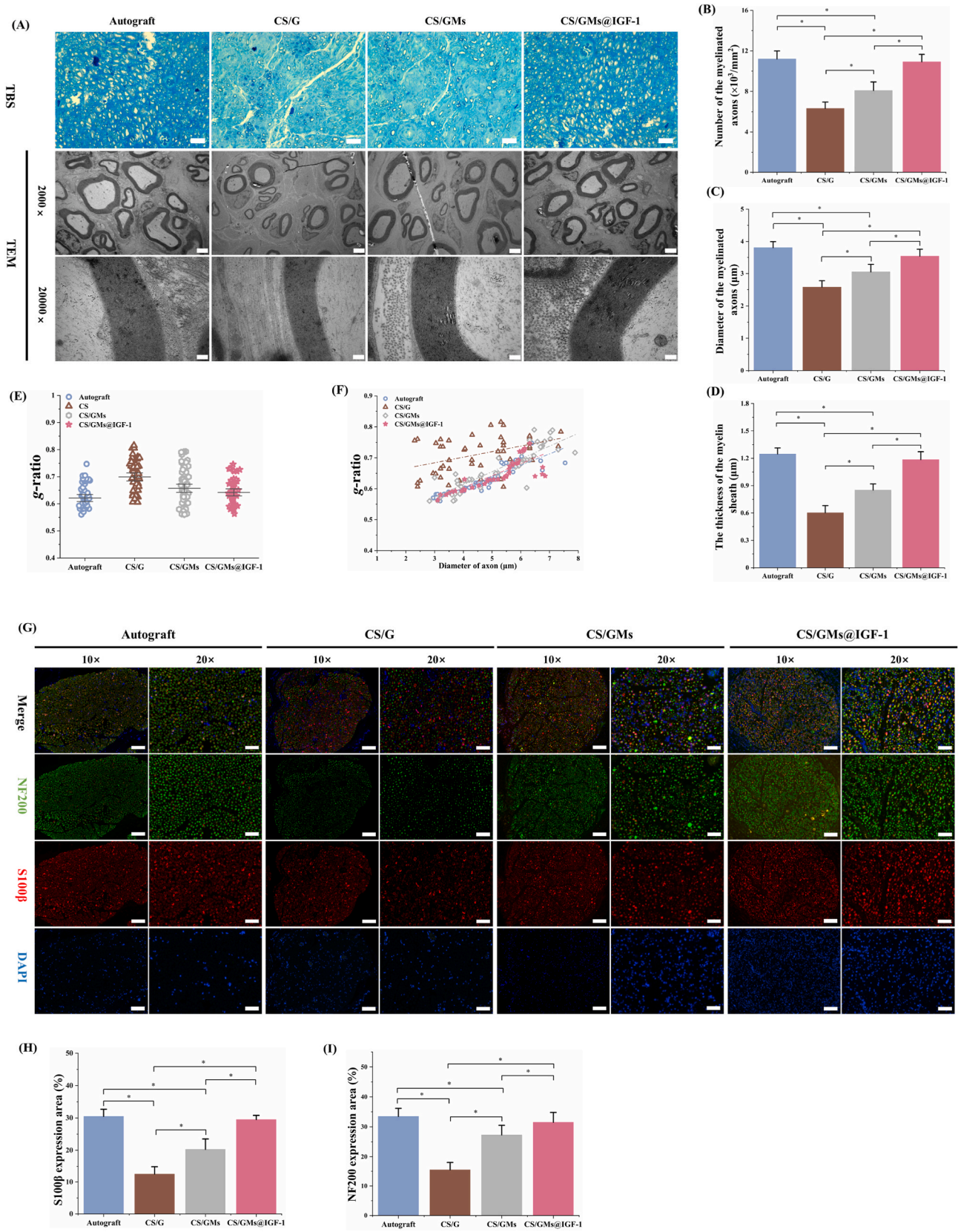

Fig. 6. Evaluation of regenerated peripheral nerves at 12 w post-implantation of the biomimetic ECM nerve conduit. (A) TB-stained and TEM images of regenerated nerves taken from 2 mm distal to the nerve conduit. Scale bars = 20 μm, 1 μm and 200 nm. (B) Quantitative analysis of myelinated nerve fiber density from the toluidine TB-stained images. (C, D) Quantitative analysis of the diameter and myelin thickness of myelinated nerve fibers from the TEM images. (E) Statistical analysis of the *g*-ratio based on the diameter. (F) Scatter plot of the *g*-ratio versus axon diameter. (G) Representative IF images of regenerated axons (NF200, green) and remyelinated nerves (S100β, red). Scale bars = 100 μm. (H, I) Quantitative analysis of regenerated axons and remyelinated nerves. Data are expressed as mean ± SD. n = 5 per group. $p^{*}<0.05$.

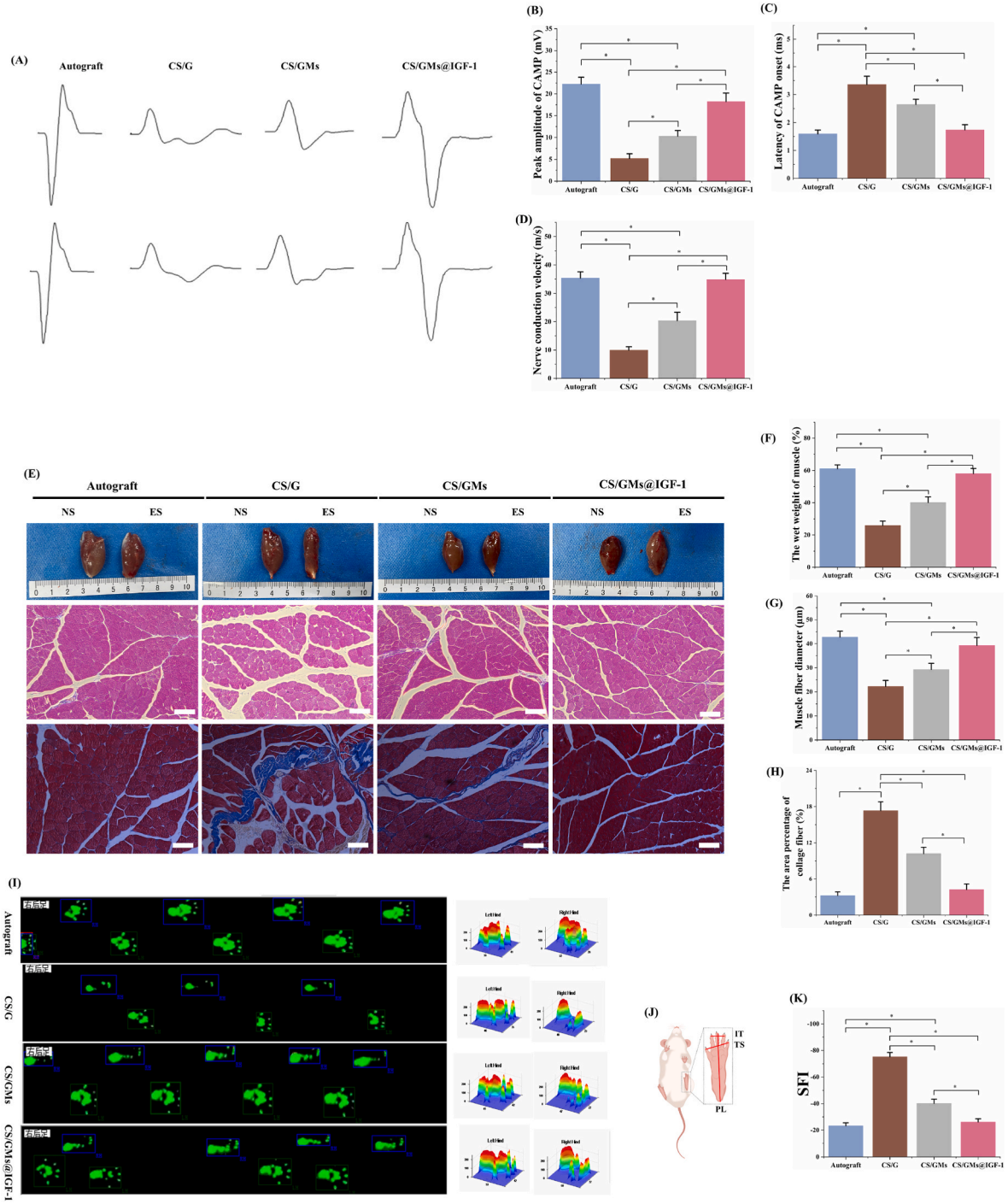

Fig. 7. Functional evaluation of regenerated nerves and gastrocnemius muscle at 12 w post-implantation of the 3D interconnected porous network with sustained IGF-1 delivery nerve conduit. (A) Representative CMAP recordings from the experimental side. Electrical stimulation (0.2 mA, 1 Hz, 0.1 ms) was applied to the proximal and distal nerve stumps of rats. (B, C, D) Quantitative analysis of nerve conduction latency, CMAP amplitude, and NCV on the experimental side. (E) Representative images of the experimental side (ES) and normal side (NS) gastrocnemius muscle, and representative microscopy images of H&E and Masson's trichrome-stained cross-sections of the experimental side gastrocnemius muscle. Scale bars = 100 μm. (F) Quantitative analysis of the wet weight ratio of the gastrocnemius muscle. (G) Statistical analysis of the mean cross-sectional area of gastrocnemius muscle fibers. (H) Automatic collection of footprints and gait using the CatWalk gait analysis system. (I) Definition of parameters used to calculate the SFI. (J, K) Quantitative analysis of the SFI. Data are expressed as mean ± SD. n = 11 per group. $p^*<0.05$.

interconnected porous structure group, the CS/GMs group had higher expression of NF200 and S100β, which was confirmed by quantitative IF intensity analysis (Fig. 6H and I), indicating the 3D interconnected porous network in nerve conduits can promote the regeneration and remyelination of axons. Consistent with the results of TEM and TB staining, it was found that the CS/GMs@IGF-1 group had similar IF expression intensity of NF200 and S100β as the Autograft group, which was significantly higher than the CS/GMs group and CS/G group, indicating the promoting effect of IGF-1 delivery on regenerating nerve.

The data obtained indicate that biomimetic ECM NGCs with a 3D interconnected porous network and sustained IGF-1 delivery support nerve regeneration at the histological level in a manner equivalent to

that of autografts.

3.7. Improvement in functional recovery of the sciatic nerve in long-term implantation by biomimetic ECM NGCs

The ultimate goal of peripheral nerve repair after injury is to restore electrophysiological conduction and motor function. This recovery can objectively evaluate the efficacy of the prepared tissue-engineered NGCs, clearly demonstrating successful nerve repair. The representative CMAP curves are shown in Fig. 7A. Quantitative analysis of the CMAP peak amplitude (Fig. 7B) revealed that the injured side in the CS/GMs@IGF-1 group (18.25 ± 1.94 mV) was significantly higher than in the CS/GMs (10.31 ± 1.03 mV) and CS/G (5.23 ± 1.06 mV) groups, approaching the Autograft group (22.24 ± 1.57 mV). This indicates that the CS/GMs@IGF-1 group had more nerve fibres innervating the muscles. Notably, a comparison of the peak amplitude of CMAP in the CS/GMs and CS/G groups showed that the 3D interconnected porous network in nerve conduits could increase nerve fibre innervation of the muscle. Similarly, the CS/GMs@IGF-1 group (1.73 ± 0.19 ms) had conduction latency (Fig. 7C) similar to the Autograft group (1.59 ± 0.14 ms, $p > 0.05$) and better than the CS/GMs and CS/G groups. Furthermore, the CMAP latency of the CS/GMs group (2.65 ± 0.18 ms) was significantly lower than that of the CS/G group (3.36 ± 0.29 ms). Further analysis showed that the 3D interconnected porous network and sustained IGF-1 delivery enhanced the NCV of the regenerated nerve. The order of NCV (Fig. 7D) from lowest to highest was CS/G (9.97 ± 1.19 m/s), CS/GMs (20.37 ± 2.94 m/s), CS/GMs@IGF-1 (34.89 ± 2.19 m/s), and Autograft (35.42 ± 2.14 m/s). The results of the CMAP peak amplitude, CMAP latency, and NCA suggested that the 3D interconnected porous network and sustained IGF-1 delivery of the biomimetic ECM conduits could enhance myelination of the regenerated nerve.

Pathological changes in the structure and function of the gastrocnemius muscle after PNI can be used to indirectly evaluate peripheral nerve regeneration. To evaluate muscle atrophy quantitatively, the muscle weight ratio was calculated by comparing the muscle on the lesioned side with that on the non-lesioned side. As confirmed in Fig. 7E and F, no measurable difference was identified between the CS/GMs@IGF-1 and Autograft groups in the gastrocnemius wet weight ratio, which were 60.1 ± 2.4 % and 58.0 ± 3.2 %, respectively. The wet weight ratio of the gastrocnemius muscle in the CS/GMs group (40.1 ± 3.5 %) was higher than that in the CS/G group (25.8 ± 2.8 %), but worse than that in the CS/GMs@IGF-1 group. Cross-sectional H&E and Masson-trichrome staining (Fig. 7E) showed that there was no obvious degradation of gastrocnemius muscle fibres in the CS/GMs@IGF-1 group (39.3 ± 3.3 μm) and Autograft group (42.7 ± 2.5 μm), and the diameter (Fig. 7G) was significantly higher than that in the CS/GMs and CS/G groups. Masson-trichrome staining results (Fig. 7H) indicated that the CS/G group exhibited extensive collagen deposition in the atrophied muscle fibers, while collagen deposition was significantly reduced in both the CS/GMs@IGF-1 group and the autologous nerve graft group. However, the gastrocnemius muscle of the CS/GMs and CS/G groups showed atrophy to a certain extent, but the CS/GMs group (29.3 ± 2.6 μm) retained more gastrocnemius muscle fibres than the CS group with closed, non-interconnected nerve conduits (22.3 ± 2.5 μm). The wet weight ratio of the gastrocnemius muscle and the pathological examination of the muscle fibres showed that biomimetic ECM nerve conduits with an interconnected porous network and sustained IGF-1 delivery could prevent muscle atrophy after PNI.

Gait analysis and footprints (Fig. 7I) were used to evaluate the recovery of motor function in rats. The SFI was calculated from the footprints to evaluate sciatic nerve function. After 12 w, the SFI (Fig. 7K) of each group from poor to excellent was as follows: Autograft (−23.3 ± 2.2), CS/GMs@IGF-1 (−26.2 ± 2.4), CS/GMs (−40.2 ± 3.2), and CS/G (−72.5 ± 3.2). It can be found that the SFI value of the Autograft group and CS/GMs@IGF-1 was almost the same and significantly higher than that of CS/GMs and CS/G. Moreover, the SFI value of the CS/GMs group was higher than that of the closed, non-interconnected, porous structure group. The representative images of 3D stress diagrams are shown in Fig. 7I, in which the stress area of the right hind limb in the CS/GMs@IGF-1 group was similar to that of the autograft group but larger than that of the CS/G and CS/GMs groups. Moreover, the CS/GMs group, which had a 3D interconnected porous network, had a larger right hindfoot stress area than the CS/G group.

Taken together, these measurements further support the hypothesis that biomimetic ECM-conduits with 3D interconnected porous networks and sustained IGF-1 delivery facilitate the recovery of motor function following sciatic nerve defects.

4. Discussion

Recent developments in tissue-engineered NGCs have focused on enhancing structural and functional capabilities [6]. Advances in 3D porous structures have significantly improved the effectiveness of these conduits by providing scaffolds that closely mimic the ECM and facilitate cell adhesion, migration, and nutrient exchange [46]. Additionally, the incorporation of IGF-1 into these conduits enhances neurotrophic support, thereby promoting nerve regeneration and functional recovery [28]. Collectively, these advancements optimise peripheral nerve repair and offer promising prospects for improved clinical outcomes in patients with nerve injuries [3]. Therefore, we developed a biomimetic ECM nerve conduit with a 3D interconnected porous network and sustained IGF-1 delivery to provide an optimal supportive microenvironment and dynamic immune modulation for nerve regeneration. By utilising the different hydrolytic properties and zeta potentials of GMs with varying degrees of cross-linking, a multifunctional GM system was established to achieve a 3D interconnected porous network and sustained delivery of IGF-1. The CL-4h GMs were completely hydrolysed and dissolved within approximately 24 h, and they were used as a sacrificial template in combination with freeze-drying to fabricate a highly porous 3D interconnected porous biomimetic ECM network structure. The 3D interconnected porous network structure allowed for a higher efficiency of substance exchange between the inside and outside of the nerve conduit wall. Sustained delivery of IGF-1 was achieved using GMs cross-linked for 24 h, which had a slower degradation rate and higher zeta potential.

The good biocompatibility, promising translational potential, and clinical operability of the fabricated NGCs are still being emphasised [47]. The materials used to prepare the nerve conduits must have good biocompatibility and be FDA-approved to ensure complete degradation without biotoxicity. The CS, gelatin, and IGF-1 used in this study have been approved by the FDA for use in tissue engineering scaffolds and medical devices [48]. In this study, the biomimetic ECM nerve conduit exhibited good biocompatibility. Twelve weeks after implantation, HE staining (Supplementary Fig. 3) of the heart, liver, spleen, lungs, and kidneys showed no abnormalities. An ideal nerve conduit should have a degradation cycle that matches the physiological processes of nerve regeneration. It should provide structural support and protection for injured peripheral nerves after implantation while avoiding compression of newly regenerated nerve fibres owing to a slow degradation rate [49]. Although nerve conduits prepared from CS and gelatin have good biocompatibility, their slow degradation is a significant drawback in clinical applications [5]. Since the repair of approximately 10 mm peripheral nerve defects typically requires around 6 months, nerve conduits that degrade by 50 % within 3 months were prepared by combining CS with multifunctional GMs at a mass ratio of 1:0.75. However, it is important to note that repairing longer peripheral nerve defects (40–50 mm) would require nerve conduits with slower degradation rates to align with the physiological timeline of peripheral nerve regeneration. Further investigation is needed to determine the optimal doping ratio of gelatin microcapsules in nerve conduits for these applications. Exploring larger nerve gap models remains a limitation of this study and represents a key direction for future research. Additionally,

the suture tensile and 50 % radial compression mechanical properties of the nerve conduits must be considered in clinical applications [50]. A nerve conduit with strong suture tensile strength and elongation at break effectively prevents the suture from breaking through the conduit wall when suturing injured peripheral nerves, making the operation easier for the surgeon [51]. The 50 % radial compressive performance of the nerve conduit ensures it does not easily deform when squeezed by surrounding tissues, maintaining its original circular structure and preventing compression or blockage of regenerating nerve tissue [52]. In this study, genipin-crosslinked GMs were incorporated into CS as a reinforcing phase. A nerve conduit with enhanced mechanical properties was constructed through the stress interface between the GMs and CS. In practical applications, the swelling rate of the hydrophilic polymer conduits must also be thoroughly considered. Excessive swelling of nerve conduits may compress or damage the surrounding nerves, causing pain, abnormal sensation, or even functional impairment [53]. The composite nerve conduit prepared with genipin-cross-linked GMs in this study exhibited a significantly lower water-absorption swelling rate than the control group prepared with homogenously blended gelatin and CS. This effectively mitigates the risk of potential compression of newly regenerated nerves. These results indicated that the multifunctional GM-CS biomimetic ECM nerve conduit developed in this study exhibits a favorable degradation rate, water swelling capacity, suture tensile strength, elongation at break, bending strength and 50 % radial compression performance, demonstrating strong clinical operability and translational potential.

Peripheral nerve regeneration is a complex process that relies on the interaction between SCs, macrophages, and axons within a supportive microenvironment [54]. After PNI, Wallerian degeneration occurs, where the distal nerve fibres degrade [55]. SCs are activated into a repair-supportive state, clearing debris and creating a favorable environment for axonal regrowth [56]. These activated SCs release cytokines to recruit macrophages to the injury site, a process that peaks three days after injury [57]. Macrophages then assist in Wallerian degeneration and polarise to the M2 pro-healing phenotype, promoting SC proliferation and migration through the secretion of neurotrophic factors [58]. SCs proliferate, form the “Büngner band,” and guide regenerating axons [59]. Successful nerve regeneration depends on reestablishing functional connectivity between regenerated axons and their target tissues [60], with SCs and macrophages coordinating inflammation resolution and regeneration [61]. The biomimetic ECM-nerve conduit prepared in this study exhibited excellent biocompatibility and promoted SC survival at the implantation site after PNI. The 3D interconnected porous network and sustained delivery of IGF-1 promoted the early functionalisation of SCs and axon outgrowth along the Büngner band to the distal target organ. Early activated SCs recruited macrophages through chemokine release, while the conduit influenced macrophage polarisation towards the M2 phenotype, supporting SC migration and remyelination. The 3D interconnected porous network with the IGF-1 delivery nerve conduit prepared in this study can provide a repair-supportive microenvironment for nerve regeneration, and its biofunction meets the requirements of the physiological processes of peripheral nerve regeneration.

Research is increasingly focusing on biomaterials and scaffold designs that can influence immune cell behaviour and provide a conducive environment for nerve healing [19]. Previous studies [62] have shown that the architecture of porous scaffolds significantly influences the immune response and subsequent tissue regeneration. For example, studies [37] have found that the infiltration of macrophages at the material-tissue interface of nonporous scaffolds is dominated by M1 macrophages, whereas porous materials respond to a significant increase in M2 macrophages. Here, we found that the 3D interconnectivity of porous nerve conduit structures plays an important role in regulating the immunophenotypic polarisation of infiltrating macrophages. The 3D interconnected porous network structures promoted the transformation of macrophages to the M2 immunophenotype, whereas the isolated porous structures did not. According to previous studies [20,63,64], the 3D interconnected porous network structure can promote macrophage polarisation towards the M2 immune phenotype through the following pathways. First, 3D interconnected porous network structures facilitate the infiltration and distribution of macrophages, promoting a more uniform and effective immune response [37]. These structures allow for better nutrient and waste exchange and reduce hypoxia and inflammation, which are conducive to the M2 macrophage phenotype. Moreover, physical cues provided by the ECM architecture can influence macrophage adhesion, spreading, and polarisation through mechanotransduction pathways [22]. In contrast, isolated, non-interconnected pore structures can create localised environments in which nutrient diffusion is restricted and cellular communication is limited. These conditions can lead to persistent inflammation and a predominance of the M1 macrophage phenotype due to hypoxic stress and the accumulation of inflammatory mediators [65]. The lack of interconnected pathways in these structures can hinder transition to the M2 phenotype, thereby impeding the healing process. Therefore, when constructing a 3D porous structure, tissue engineering scaffolds must consider the interconnectedness, openness, and permeability of the pores to optimise macrophage-mediated immune responses. To further enhance the regulation of macrophage immune phenotypes and provide a reparative-supportive microenvironment for peripheral nerve regeneration, IGF-1, a multifunctional peptide hormone, was encapsulated in the gelatin microcapsules for sustained release at the injury site. Previous studies [66,67] have shown that IGF-1 exerts its effects on macrophages through several mechanisms. It modulates the expression of surface receptors and intracellular signalling pathways that dictate macrophage behaviour. Recent studies indicate that IGF-1 promotes the M2 phenotype, characterised by the expression of anti-inflammatory cytokines such as IL-10 and TGF-β and surface markers including CD206 and Arg1 [68]. Mechanistically, IGF-1 signalling through the IGF-1 receptor activates downstream pathways, notably the PI3K/Akt and ERK1/2 cascades, which are pivotal in driving M2 polarisation [69–71]. In this study, dynamic regulation of macrophage immune phenotypes was achieved through a tailored interconnected porous 3D network structure and sustained delivery of IGF-1, thereby creating a favorable immune microenvironment for peripheral nerve regeneration.

In summary, the biomimetic ECM NGC developed in this study fully meets the practical requirements for clinical applications, is easy to handle, and has excellent potential for clinical translation. In terms of promoting nerve regeneration, the NGCs achieve therapeutic effects comparable to those of autologous nerve grafts, demonstrating significant potential as a new therapeutic strategy.

5. Conclusion

In this study, biomimetic ECM NGCs, featuring a 3D interconnected porous network and sustained delivery of IGF-1, were developed by integrating multi-functional GMs with CS to enhance nerve regeneration. GMs with two degrees of cross-linking (CL-4h and CL-24h) were used as sacrificial templates to construct a 3D interconnected porous structure and load IGF-1. The incorporation of multi-functional GMs into the NGCs maintained the honeycomb-like structure, improved the interconnectedness of the porous structure, and enhanced the permeability and substance exchange. The optimal CS:0.75 GMs formulation demonstrated superior suture tensile strength, elongation at break, 50 % radial compression, bending strength, an appropriate water absorption swelling rate, and a degradation period consistent with the 6-month nerve regeneration cycle, showing strong clinical operability and translational potential. In terms of bio-functionality, the biomimetic ECM NGCs promoted the survival, proliferation, and remyelination potential of SCs, along with neurite formation, providing a supportive microenvironment for peripheral nerve regeneration that met physiological requirements. Additionally, the 3D interconnected porous structure and sustained delivery of IGF-1 facilitated macrophage

recruitment and M2 immune phenotype polarisation, thereby enhancing SC migration and differentiation after PNI, along with improved motor and sensory function recovery. This study demonstrates that the biomimetic ECM NGC, with its 3D interconnected porous structure and sustained IGF-1 delivery, is a potential material for achieving rapid regeneration after PNI, offering an alternative to autologous nerve grafts.

CRediT authorship contribution statement

Teng Wan: Writing – original draft, Visualization, Software, Methodology, Investigation, Formal analysis, Data curation, Conceptualization. **Qi-Cheng Li:** Formal analysis. **Feng-Shi Zhang:** Software, Data curation. **Xiao-Meng Zhang:** Investigation. **Na Han:** Supervision, Writing – review & editing. **Pei-Xun Zhang:** Writing – review & editing, Supervision, Resources, Project administration, Methodology, Funding acquisition.

Ethics approval and consent to participate

All animal experiments were performed after the approvement of the Animal Experimental Ethics Committee of Peking University People's Hospital complied with the requirements of the National Institutes of Health Guide for the Care and Use of Laboratory Animals.

Declaration of Competing interest

The authors declare that they have no conflict of interest.

Acknowledgements

This research was financially supported by the National Natural Science Foundation of China (Project:22278003); the Cross-cooperation project of Beijing Science and Technology New Star Program (Project: 20220484233); Peking University People's Hospital Research and Development Fund (RDH2020-01).

Appendix A. Supplementary data

Supplementary data to this article can be found online at https://doi.org/10.1016/j.mtbio.2024.101403.

Data availability

Data will be made available on request.

References

[1] A. Escobar, A. Serafin, M.R. Carvalho, M. Culebras, A. Cantarero, A. Beaucamp, R. L. Reis, J.M. Oliveira, M.N. Collins, Electroconductive poly(3,4-ethylenedioxythiophene) (PEDOT) nanoparticle-loaded silk fibroin biocomposite conduits for peripheral nerve regeneration, Advanced Composites and Hybrid Materials 6 (3) (2023) 118. https://10.1007/s42114-023-00689-2.

[2] V.K. Sundaram, V. Schütza, N.H. Schröter, A. Backhaus, A. Bilsing, L. Joneck, A. Seelbach, C. Mutschler, J.A. Gomez-Sanchez, E. Schäffner, E.E. Sánchez, D. Akkermann, C. Paul, N. Schwagarus, S. Müller, A. Odle, G. Childs, D. Ewers, T. Kungl, M. Sitte, G. Salinas, M.W. Sereda, K.-A. Nave, M.H. Schwab, M. Ost, P. Arthur-Farraj, R.M. Stassart, R. Fledrich, Adipo-glial signaling mediates metabolic adaptation in peripheral nerve regeneration, Cell Metabol. 35 (12) (2023) 2136–2152.e9. https://10.1016/j.cmet.2023.10.017.

[3] W. Zhou, M.S.U. Rahman, C. Sun, S. Li, N. Zhang, H. Chen, C.C. Han, S. Xu, Y. Liu, Perspectives on the novel multifunctional nerve guidance conduits: from specific regenerative procedures to motor function rebuilding, Adv. Mater. 36 (14) (2024) 2307805. https://10.1002/adma.202307805.

[4] Y. Fang, C. Wang, Z. Liu, J. Ko, L. Chen, T. Zhang, Z. Xiong, L. Zhang, W. Sun, 3D printed conductive multiscale nerve guidance conduit with hierarchical fibers for peripheral nerve regeneration, Adv. Sci. 10 (12) (2023) 2205744. https://10.1002/advs.202205744.

[5] H. Zhang, J. Guo, Y. Wang, L. Shang, R. Chai, Y. Zhao, Natural polymer-derived bioscaffolds for peripheral nerve regeneration, Adv. Funct. Mater. 32 (41) (2022) 2203829. https://10.1002/adfm.202203829.

[6] C. Zhang, J. Gong, J. Zhang, Z. Zhu, Y. Qian, K. Lu, S. Zhou, T. Gu, H. Wang, Y. He, M. Yu, Three potential elements of developing nerve guidance conduit for peripheral nerve regeneration, Adv. Funct. Mater. 33 (40) (2023) 2302251. https://10.1002/adfm.202302251.

[7] Y. Wang, Z. Yan, W. Liu, C. Liu, N. Xu, Y. Wu, F. Sun, X. Wang, Y. Qian, L. Jiang, X. Sun, Biomechanically-adapted immunohydrogels reconstructing myelin sheath for peripheral nerve regeneration, Adv. Healthcare Mater. 11 (20) (2022) 2201596. https://10.1002/adhm.202201596.

[8] Q. Wang, Y. Wei, X. Yin, G. Zhan, X. Cao, H. Gao, Engineered PVDF/PLCL/PEDOT Dual Electroactive Nerve Conduit to Mediate Peripheral Nerve Regeneration by Modulating the Immune Microenvironment, Adv. Funct. Mater. n/a(n/a)2400217. https://10.1002/adfm.202400217.

[9] C.B. Xue, H. Zhu, H.K. Wang, Y.X. Wang, X. Xu, S.L. Zhou, D. Liu, Y.H. Zhao, T. M. Qian, Q. Guo, J. He, K.R. Zhang, Y. Gu, L.L. Gong, J. Yang, S. Yi, B. Yu, Y. J. Wang, Y. Liu, Y.M. Yang, F. Ding, X.S. Gu, Skin derived precursors induced Schwann cells mediated tissue engineering-aided neuroregeneration across sciatic nerve defect, Bioact. Mater. 33 (2024) 572–590. https://10.1016/j.bioactmat.2023.11.016.

[10] T. Ma, Y. Hao, S. Li, B. Xia, X. Gao, Y. Zheng, L. Mei, Y. Wei, C. Yang, L. Lu, Z. Luo, J. Huang, Sequential oxygen supply system promotes peripheral nerve regeneration by enhancing Schwann cells survival and angiogenesis, Biomaterials 289 (2022) 121755. https://10.1016/j.biomaterials.2022.121755.

[11] Y. Li, S. Lv, H. Yuan, G. Ye, W. Mu, Y. Fu, X. Zhang, Z. Feng, Y. He, W. Chen, Peripheral nerve regeneration with 3D printed bionic scaffolds loading neural crest stem cell derived schwann cell progenitors, Adv. Funct. Mater. 31 (16) (2021) 2010215. https://10.1002/adfm.202010215.

[12] Y.H. Li, S. Kang, D. Halawani, Y.Q. Wang, C.J. Alves, A. Ramakrishnan, M. Estill, L. Shen, F.T. Li, X.J. He, R.H. Friedel, H.Y. Zou, Macrophages facilitate peripheral nerve regeneration by organizing regeneration tracks through Plexin-B2, Gene Dev. 36 (3–4) (2022) 133–148. https://10.1101/gad.349063.121.

[13] P. Yang, Y. Peng, X. Dai, J. Jie, D. Kong, X. Gu, Y. Yang, Bionic peptide scaffold in situ polarization and recruitment of M2 macrophages to promote peripheral nerve regeneration, Bioact. Mater. 30 (2023) 85–97. https://10.1016/j.bioactmat.2023.07.003.

[14] J.A. Fissel, M.H. Farah, The influence of BACE1 on macrophage recruitment and activity in the injured peripheral nerve, J. Neuroinflammation 18 (1) (2021) 71. https://10.1186/s12974-021-02121-2.

[15] P.K. Govindappa, J.C. Elfar, Erythropoietin promotes M2 macrophage phagocytosis of Schwann cells in peripheral nerve injury, Cell Death Dis. 13 (3) (2022) 245. https://10.1038/s41419-022-04671-6.

[16] J. Xu, J. Wen, L. Fu, L. Liao, Y. Zou, J. Zhang, J. Deng, H. Zhang, J. Liu, X. Wang, D. Zuo, J. Guo, Macrophage-specific RhoA knockout delays Wallerian degeneration after peripheral nerve injury in mice, J. Neuroinflammation 18 (1) (2021) 234. https://10.1186/s12974-021-02292-y.

[17] J.-Y. Wang, Y. Yuan, S.-Y. Zhang, S.-Y. Lu, G.-J. Han, M.-X. Bian, L. huang, D.-H. Meng, D.-H. Su, L. Xiao, Y. Xiao, J. Zhang, N.-J. Gong, L.-B. Jiang, Remodeling of the intra-conduit inflammatory microenvironment to improve peripheral nerve regeneration with a neuromechanical matching protein-based conduit, Adv. Sci. 11 (17) (2024) 2302988. https://10.1002/advs.202302988.

[18] Y. Gao, Y. Wang, J. Zhang, M. Zhang, C. Dai, Y. Zhang, L. Zhang, L. Bian, Y. Yang, K. Zhang, Y. Zhao, Advancing neural regeneration via adaptable hydrogels: enriched with Mg2+ and silk fibroin to facilitate endogenous cell infiltration and macrophage polarization, Bioact. Mater. 33 (2024) 100–113. https://10.1016/j.bioactmat.2023.10.026.

[19] Q. Yang, S. Su, S. Liu, S. Yang, J. Xu, Y. Zhong, Y. Yang, L. Tian, Z. Tan, J. Wang, Z. Yu, Z. Shi, F. Liang, Exosomes-loaded electroconductive nerve dressing for nerve regeneration and pain relief against diabetic peripheral nerve injury, Bioact. Mater. 26 (2023) 194–215. https://10.1016/j.bioactmat.2023.02.024.

[20] X. Dong, S. Liu, Y. Yang, S. Gao, W. Li, J. Cao, Y. Wan, Z. Huang, G. Fan, Q. Chen, H. Wang, M. Zhu, D. Kong, Aligned microfiber-induced macrophage polarization to guide schwann-cell-enabled peripheral nerve regeneration, Biomaterials 272 (2021) 120767. https://10.1016/j.biomaterials.2021.120767.

[21] L.D.V. Johnson, M. Aleemardani, S. Atkins, F.M. Boissonade, F. Claeyssens, Emulsion templated composites: porous nerve guidance conduits for peripheral nerve regeneration, Mater. Des. 239 (2024) 112779. https://10.1016/j.matdes.2024.112779.

[22] Z. Chen, J. Zheng, X. Pei, S. Sun, J. Cai, Y. Liu, Y. Wang, L. Zheng, H. Zhou, Ultrasound-driven electrical stimulation based on 3D hierarchical porous piezoelectric nanofiber-aerogel scaffold promotes bone defect repair, Chem. Eng. J. 470 (2023) 144305. https://10.1016/j.cej.2023.144305.

[23] H. Zhang, H. Zhang, H. Wang, Y. Zhao, R. Chai, Natural proteins-derived asymmetric porous conduit for peripheral nerve regeneration, Appl. Mater. Today 27 (2022) 101431. https://10.1016/j.apmt.2022.101431.

[24] Z. Cai, Y. Tang, Y. Wei, P. Wang, H. Zhang, Double – network hydrogel based on exopolysaccharides as a biomimetic extracellular matrix to augment articular cartilage regeneration, Acta Biomater. 152 (2022) 124–143. https://10.1016/j.actbio.2022.08.062.

[25] P.R.L. Dabare, A. Bachhuka, J.Y. Quek, L.F. Marsal, J. Hayball, K. Vasilev, Nano-roughness-mediated macrophage polarization for desired host immune response, Small Science 3 (10) (2023) 2300080. https://10.1002/smsc.202300080.

[26] N. Kartikasari, M. Yamada, J. Watanabe, W. Tiskratok, X. He, Y. Kamano, H. Egusa, Titanium surface with nanospikes tunes macrophage polarization to produce inhibitory factors for osteoclastogenesis through nanotopographic cues, Acta Biomater. 137 (2022) 316–330. https://10.1016/j.actbio.2021.10.019.

[27] G.W. Zhu, R.Y. Zhang, Q.Y. Xie, P.L. Li, F.J. Wang, L. Wang, C.J. Li, Shish-kebab structure fiber with nano and micro diameter regulate macrophage polarization for

anti-inflammatory and bone differentiation, Mater Today Bio 23 (2023). https://10.1016/j.mtbio.2023.100880.
[28] P.J. Hanwright, C. Qiu, J. Rath, Y. Zhou, N. von Guionneau, K.A. Sarhane, T.G. W. Harris, G.P. Howard, H. Malapati, M.J. Lan, S. Reddy, A. Hoke, H.-Q. Mao, S. H. Tuffaha, Sustained IGF-1 delivery ameliorates effects of chronic denervation and improves functional recovery after peripheral nerve injury and repair, Biomaterials 280 (2022) 121244. https://10.1016/j.biomaterials.2021.121244.
[29] T. Wan, F.-S. Zhang, M.-Y. Qin, H.-R. Jiang, M. Zhang, Y. Qu, Y.-L. Wang, P.-X. Zhang, Growth factors: bioactive macromolecular drugs for peripheral nerve injury treatment – molecular mechanisms and delivery platforms, Biomed. Pharmacother. 170 (2024) 116024. https://10.1016/j.biopha.2023.116024.
[30] H. Xu, Z. Gao, Z. Wang, W. Wu, H. Li, Y. Liu, S. Jia, D. Hao, L. Zhu, Electrospun PCL nerve conduit filled with GelMA gel for CNTF and IGF-1 delivery in promoting sciatic nerve regeneration in rat, ACS Biomater. Sci. Eng. 9 (11) (2023) 6309–6321. https://10.1021/acsbiomaterials.3c01048.
[31] J. Zhang, Y. Zhang, Y.K. Jiang, J.A. Li, W.F. Wei, M.P. Shi, Y.B. Wang, G.L. Jia, The effect of poly(lactic-co-glycolic acid) conduit loading insulin-like growth factor 1 modified by a collagen-binding domain on peripheral nerve injury in rats, J. Biomed. Mater. Res. B Appl. Biomater. 110 (9) (2022) 2100–2109. https://10.1002/jbm.b.35064.
[32] X. Shan, P. Hu, L. Ni, L. Shen, Y. Zhang, Z. Ji, Y. Cui, M. Guo, H. Wang, L. Ran, K. Yang, T. Wang, L. Wang, B. Chen, Z. Yao, Y. Wu, Q. Yu, Serine metabolism orchestrates macrophage polarization by regulating the IGF1–p38 axis, Cell. Mol. Immunol. 19 (11) (2022) 1263–1278. https://10.1038/s41423-022-00925-7.
[33] B.R. Slavin, K.A. Sarhane, N. von Guionneau, P.J. Hanwright, C. Qiu, H.-Q. Mao, A. Höke, S.H. Tuffaha, Insulin-like growth factor-1: a promising therapeutic target for peripheral nerve injury, Front. Bioeng. Biotechnol. 9 (2021). https://10.3389/fbioe.2021.695850.
[34] Y. Endo, M. Samandari, M. Karvar, A. Mostafavi, J. Quint, C. Rinoldi, I.K. Yazdi, W. Swieszkowski, J. Mauney, S. Agarwal, A. Tamayol, I. Sinha, Aerobic exercise and scaffolds with hierarchical porosity synergistically promote functional recovery post volumetric muscle loss, Biomaterials 296 (2023) 122058. https://10.1016/j.biomaterials.2023.122058.
[35] H. Wang, R. Yu, M. Wang, S. Wang, X. Ouyang, Z. Yan, S. Chen, W. Wang, F. Wu, C. Fan, Insulin-like growth factor binding protein 4 loaded electrospun membrane ameliorating tendon injury by promoting retention of IGF-1, J. Contr. Release 356 (2023) 162–174. https://10.1016/j.jconrel.2023.02.039.
[36] P. Wang, X. Meng, R. Wang, W. Yang, L. Yang, J. Wang, D.-A. Wang, C. Fan, Biomaterial scaffolds made of chemically cross-linked gelatin microsphere aggregates (C-GMSs) promote vascularized bone regeneration, Adv. Healthcare Mater. 11 (13) (2022) 2102818. https://10.1002/adhm.202102818.
[37] J.L. Hernandez, K.A. Woodrow, Medical applications of porous biomaterials: features of porosity and tissue-specific implications for biocompatibility, Adv. Healthcare Mater. 11 (9) (2022) 2102087. https://10.1002/adhm.202102087.
[38] F.J. Maksoud, M.F. Velázquez de la Paz, A.J. Hann, J. Thanarak, G.C. Reilly, F. Claeyssens, N.H. Green, Y.S. Zhang, Porous biomaterials for tissue engineering: a review, J. Mater. Chem. B 10 (40) (2022) 8111–8165. https://10.1039/D1TB02628C.
[39] R.T. Annamalai, P.A. Turner, W.F. Carson, B. Levi, S. Kunkel, J.P. Stegemann, Harnessing macrophage-mediated degradation of gelatin microspheres for spatiotemporal control of BMP2 release, Biomaterials 161 (2018) 216–227. https://10.1016/j.biomaterials.2018.01.040.
[40] F. Sabbagh, A.R. Deshmukh, Y. Choi, B.S. Kim, Effect of microsphere concentration on catechin release from microneedle arrays, ACS Appl. Mater. Interfaces 16 (22) (2024) 28276–28289. https://10.1021/acsami.4c06064.
[41] Q.-R. Jiang, X.-Q. Pu, C.-F. Deng, W. Wang, Z. Liu, R. Xie, D.-W. Pan, W.-J. Zhang, X.-J. Ju, L.-Y. Chu, Microfluidic controllable preparation of iodine-131-labeled microspheres for radioembolization therapy of liver tumors, Adv. Healthcare Mater. 12 (21) (2023) 2300873. https://10.1002/adhm.202300873.
[42] C. Qiao, X. Ma, J. Zhang, J. Yao, Molecular interactions in gelatin/chitosan composite films, Food Chem. 235 (2017) 45–50. https://10.1016/j.foodchem.2017.05.045.
[43] S. Zou, S. Fan, A.L. Oliveira, X. Yao, Y. Zhang, H. Shao, 3D printed gelatin scaffold with improved shape fidelity and cytocompatibility by using Antheraea pernyi silk fibroin nanofibers, Advanced Fiber Materials 4 (4) (2022) 758–773. https://10.1007/s42765-022-00135-w.
[44] X. Wu, O. Gauntlett, T. Zhang, S. Suvarnapathaki, C. McCarthy, B. Wu, G. Camci-Unal, Eggshell microparticle reinforced scaffolds for regeneration of critical sized cranial defects, ACS Appl. Mater. Interfaces 13 (51) (2021) 60921–60932. https://10.1021/acsami.1c19884.
[45] X. Yao, L. Zhan, Z. Yan, J. Li, L. Kong, X. Wang, H. Xiao, H. Jiang, C. Huang, Y. Ouyang, Y. Qian, C. Fan, Non-electric bioelectrical analog strategy by a biophysical-driven nano-micro spatial anisotropic scaffold for regulating stem cell niche and tissue regeneration in a neuronal therapy, Bioact. Mater. 20 (2023) 319–338. https://10.1016/j.bioactmat.2022.05.034.
[46] M. Sun, D. You, N. Zhan, C. Liu, X. Zhang, L. Lin, J. Zhang, Y. Lou, Y. Chen, C. Liu, H. Wang, Y. He, M. Yu, 4D oriented dynamic scaffold for promoting peripheral nerve regeneration and functional recovery, Adv. Funct. Mater. 34 (2) (2024) 2305827. https://10.1002/adfm.202305827.
[47] X. Ren, X. Chen, Z. Geng, J. Su, Bone-targeted biomaterials: strategies and applications, Chem. Eng. J. 446 (2022) 137133. https://10.1016/j.cej.2022.137133.
[48] M. Oprea, S.I. Voicu, Recent advances in composites based on cellulose derivatives for biomedical applications, Carbohydrate Polymers 247 (2020) 116683. https://10.1016/j.carbpol.2020.116683.
[49] J. Kim, J. Park, G. Choe, S.-I. Jeong, H.-S. Kim, J.Y. Lee, A Gelatin/Alginate Double Network Hydrogel Nerve Guidance Conduit Fabricated by a Chemical-Free Gamma Radiation for Peripheral Nerve Regeneration, Adv. Healthcare Mater.n/a(n/a) 2400142. https://10.1002/adhm.202400142.
[50] J. Zhang, Z. Liu, J. Wang, Y. Zhang, J. Dong, J. Gao, L. Zhang, J. Wang, P. Tang, Q. Zhang, 3D coaxially printing rGO aerogel-based biocompatible fiber for peripheral nerve regeneration, Advanced Fiber Materials 6 (3) (2024) 713–726. https://10.1007/s42765-023-00352-x.
[51] S. Biggi, G.A. Bassani, V. Vincoli, D. Peroni, V. Bonaldo, M. Biagiotti, R. Belli, A. Alessandrino, E. Biasini, G. Freddi, Characterization of physical, mechanical, and biological properties of SilkBridge nerve conduit after enzymatic hydrolysis, ACS Appl. Bio Mater. 3 (12) (2020) 8361–8374. https://10.1021/acsabm.0c00613.
[52] X. Liu, J. Yan, J. Liu, Y. Wang, J. Yin, J. Fu, Fabrication of a dual-layer cell-laden tubular scaffold for nerve regeneration and bile duct reconstruction, Biofabrication 13 (3) (2021) 035038. https://10.1088/1758-5090/abf995.
[53] X. Li, W. Yang, H. Xie, J. Wang, L. Zhang, Z. Wang, L. Wang, CNT/Sericin conductive nerve guidance conduit promotes functional recovery of transected peripheral nerve injury in a rat model, ACS Appl. Mater. Interfaces 12 (33) (2020) 36860–36872. https://10.1021/acsami.0c08457.
[54] W. Cao, Y. Zhang, L. Li, B. Liu, J. Ding, X. Chen, Physical cues of scaffolds promote peripheral nerve regeneration, Appl. Phys. Rev. 11 (2) (2024). https://10.1063/5.0189181.
[55] R. Zhao, X. Deng, J. Dong, C. Liang, X. Yang, Y. Tang, J. Du, Z. Ge, D. Wang, Y. Shen, L. Jiang, W. Lin, T. Zhu, G. Wang, Highly bioadaptable hybrid conduits with spatially bidirectional structure for precision nerve fiber regeneration via gene therapy, Adv. Sci. 11 (19) (2024) 2309306. https://10.1002/advs.202309306.
[56] Y.R. Jo, Y. Oh, Y.H. Kim, Y.K. Shin, H.R. Kim, H. Go, J. Shin, H.J. Park, H. Koh, J. K. Kim, J.E. Shin, K.E. Lee, H.T. Park, Adaptive autophagy reprogramming in Schwann cells during peripheral demyelination, Cell. Mol. Life Sci. 80 (1) (2023) 34. https://10.1007/s00018-022-04683-7.
[57] Y. Huang, L. Wu, Y. Zhao, J. Guo, R. Li, S. Ma, Z. Ying, Schwann cell promotes macrophage recruitment through IL-17B/IL-17RB pathway in injured peripheral nerves, Cell Rep. 43 (2) (2024) 113753. https://10.1016/j.celrep.2024.113753.
[58] M.K. Jha, J.V. Passero, A. Rawat, X.H. Ament, F. Yang, S. Vidensky, S.L. Collins, M. R. Horton, A. Hoke, G.A. Rutter, A. Latremoliere, J.D. Rothstein, B.M. Morrison, Macrophage monocarboxylate transporter 1 promotes peripheral nerve regeneration after injury in mice, J. Clin. Invest. 131 (21) (2021). https://10.1172/jci141964.
[59] T. Weiss, S. Taschner-Mandl, L. Janker, A. Bileck, F. Rifatbegovic, F. Kromp, H. Sorger, M.O. Kauer, C. Frech, R. Windhager, C. Gerner, P.F. Ambros, I. M. Ambros, Schwann cell plasticity regulates neuroblastic tumor cell differentiation via epidermal growth factor-like protein 8, Nat. Commun. 12 (1) (2021) 1624. https://10.1038/s41467-021-21859-0.
[60] J. Song, B. Lv, W. Chen, P. Ding, Y. He, Advances in 3D printing scaffolds for peripheral nerve and spinal cord injury repair, Int. J. Extrem. Manuf. 5 (3) (2023) 032008. https://10.1088/2631-7990/acde21.
[61] P. Sun, Y. Guan, C. Yang, H. Hou, S. Liu, B. Yang, X. Li, S. Chen, L. Wang, H. Wang, Y. Huang, X. Sheng, J. Peng, W. Xiong, Y. Wang, L. Yin, A bioresorbable and conductive scaffold integrating silicon membranes for peripheral nerve regeneration, Adv. Healthcare Mater. 12 (32) (2023) 2301859. https://10.1002/adhm.202301859.
[62] C. Jiang, M. Ding, J. Zhang, C. Zhu, W. Qin, Z. Zhao, T. Jiao, 3D printed porous zirconia biomaterials based on triply periodic minimal surfaces promote osseointegration in vitro by regulating osteoimmunomodulation and osteo/angiogenesis, ACS Appl. Mater. Interfaces 16 (12) (2024) 14548–14560. https://10.1021/acsami.3c18799.
[63] G. Zhu, R. Zhang, Q. Xie, P. Li, F. Wang, L. Wang, C. Li, Shish-kebab structure fiber with nano and micro diameter regulate macrophage polarization for anti-inflammatory and bone differentiation, Mater Today Bio 23 (2023) 100880. https://10.1016/j.mtbio.2023.100880.
[64] T.J. Thorson, R.E. Gurlin, E.L. Botvinick, A. Mohraz, Bijel-templated implantable biomaterials for enhancing tissue integration and vascularization, Acta Biomater. 94 (2019) 173–182. https://10.1016/j.actbio.2019.06.031.
[65] X. Qin, Z. Niu, H. Chen, Y. Hu, Macrophage-derived exosomal HMGB3 regulates silica-induced pulmonary inflammation by promoting M1 macrophage polarization and recruitment, Part. Fibre Toxicol. 21 (1) (2024) 12. https://10.1186/s12989-024-00568-8.
[66] E.J. Chung, S. Kwon, J.L. Reedy, A.O. White, J.S. Song, I. Hwang, J.Y. Chung, K. Ylaya, S.M. Hewitt, D.E. Citrin, IGF-1 receptor signaling regulates type II pneumocyte senescence and resulting macrophage polarization in lung fibrosis, Int. J. Radiat. Oncol. Biol. Phys. 110 (2) (2021) 526–538. https://10.1016/j.ijrobp.2020.12.035.
[67] D.C. Ivan, K.C. Berve, S. Walthert, G. Monaco, K. Borst, E. Bouillet, F. Ferreira, H. Lee, J. Steudler, T. Buch, M. Prinz, B. Engelhardt, G. Locatelli, Insulin-like growth factor-1 receptor controls the function of CNS-resident macrophages and their contribution to neuroinflammation, Acta Neuropathologica Communications 11 (1) (2023) 35. https://10.1186/s40478-023-01535-8.
[68] M.-N. Podaru, L. Fields, S. Kainuma, Y. Ichihara, M. Hussain, T. Ito, K. Kazuya, F. D'Aquisto, A. Mathur, F. Lewis, K. Suzuki, Abstract 718: reparative macrophage transplantation for myocardial repair: a refinement of bone marrow mononuclear cell-based therapy, Circ. Res. 125 (Suppl_1) (2019) A718. A718, https://10.1161/res.125.suppl_1.718.
[69] V. Furundzija, J. Fritzsche, J. Kaufmann, H. Meyborg, E. Fleck, K. Kappert, P. Stawowy, IGF-1 increases macrophage motility via PKC/p38-dependent αvβ3-

integrin inside-out signaling, Biochem. Biophys. Res. Commun. 394 (3) (2010) 786–791. https://10.1016/j.bbrc.2010.03.072.

[70] J. Wang, L. Xie, S. Wang, J. Lin, J. Liang, J. Xu, Azithromycin promotes alternatively activated macrophage phenotype in systematic lupus erythematosus via PI3K/Akt signaling pathway, Cell Death Dis. 9 (11) (2018) 1080. https://10.1038/s41419-018-1097-5.

[71] J.M. Fritz, L.D. Dwyer-Nield, A.M. Malkinson, Stimulation of neoplastic mouse lung cell proliferation by alveolar macrophage-derived, insulin-like growth factor-1 can be blocked by inhibiting MEK and PI3K activation, Mol. Cancer 10 (1) (2011) 76. https://10.1186/1476-4598-10-76.